Atmos. Chem. Phys., 26, 11111–11133, 2026
https://doi.org/10.5194/acp-26-11111-2026


Atmospheric Chemistry and Physics
Open Access
EGU

Research article

# Elevated aerosol layers within the daytime mixed layer over ecologically sensitive areas of northwest China: diurnal variation, formation mechanisms and regional effects

**Zikai Lin[1], Tian Zhou[1], Zhengpeng Li[1], Yonghong Gu[1], Dongsheng Wu[1], Ping Zhou[3], Keyu Zhang[1], Qili Gao[1], Xingran Li[1], Zhongwei Huang[1,2], Jianrong Bi[1,2], Lili Yang[4], and Lina Wang[4]**

[1]Key Laboratory for Semi-Arid Climate Change of the Ministry of Education,
College of Atmospheric Sciences, Lanzhou University, Lanzhou 730000, China
[2]Collaborative Innovation Center for Western Ecological Safety, Lanzhou University, Lanzhou, 730000, China
[3]School of Atmospheric Sciences, Sun Yat-sen University, Zhuhai, Guangdong 519082, China
[4]Gansu Province Environmental Monitoring Center, Lanzhou 730000, China

**Correspondence:** Tian Zhou (zhoutian@lzu.edu.cn)

Received: 8 May 2026 – Discussion started: 29 May 2026
Revised: 14 July 2026 – Accepted: 29 July 2026 – Published: 10 August 2026

**Abstract.** The cyclic processes of aerosol evolution have a profound impact on regional climate, water resources and ecosystems. However, studies on diurnal variations of aerosol vertical distribution in typical ecologically sensitive areas remain scarce due to limited availability of high-resolution profiles. This study first identifies the elevated aerosol layer (EAL) embedded within the daytime mixed layer over the Hexi Corridor, northwest China, defined as a high-concentration layer above the surface but within the mixed layer. Based on intensive observation campaigns conducted in 2010 and 2012, we analyze the diurnal variation, formation mechanisms, air quality and radiative effects of EALs. The results show that EALs frequently occur at altitudes of 0.6–2 km during daytime. Excluding dust events, the occurrence frequencies were 82 % and 44 % at Dunhuang and Minqin, respectively; the layers were more frequently dust-influenced at Dunhuang and fine-mode/anthropogenic-aerosol-influenced at Minqin. Driven by a thermodynamic coupling effect characterized by positive anomalies in potential temperature and negative anomalies in relative humidity, aerosols accumulate at the bottom of the stable stratification. Thus, a simplified conceptual model for prediction is proposed. The peak Extinction-derived $PM_{10}$-equivalent mass concentration within EAL ($203.3 \pm 106.6\,\mu g\,m^{-3}$) at $\sim 1.2$ km is five times higher than that at surface ($40.8 \pm 30.4\,\mu g\,m^{-3}$). Furthermore, the EALs enhance the atmospheric shortwave heating rate (up to $0.7\,K\,d^{-1}$), indicating a potential impact on regional snowmelt/glacier retreat. These findings suggest that the aerosol vertical evolution should receive greater consideration in air pollution prevention, ecosystem protection, water resource management, and wind/solar-energy utilization in ecologically sensitive areas, particularly over complex terrains, rather than focusing solely on surface air pollution.

## 1 Introduction

Aerosols exert significant environmental and climatic impacts. Aerosol properties exhibit substantial variability across temporal and spatial scales; it is crucial to accurately characterise the three-dimensional spatiotemporal distribution of aerosols (Park and Allen, 2015; Manavi et al., 2025). The vertical distribution of aerosols is a primary factor modulating their radiative effects (Huang et al., 2014; Sun et al., 2018; Guo et al., 2022; Derepentigny, 2024; Che et al., 2024), as it directly determines their interactions with solar and outgoing longwave radiation (Liu et al., 2019; Fountoulakis et al., 2022). It also governs the deposition of light-absorbing aerosols such as dust and black carbon in high-mountain snowpacks, thereby regulating snow albedo reduction and accelerating glacial snowmelt in high-altitude regions (Sarangi et al., 2020). In addition, the vertical distribution of aerosols serves as an important indicator for assessing regional pollution levels and tracing emission sources (Huige et al., 2021; Pace et al., 2015). Furthermore, it can influence atmospheric stability, thereby affecting the development of turbulence and cloud formation (Petrovic et al., 2017; Su et al., 2020b; Li et al., 2021a; Liang et al., 2022).

To date, substantial progress has been made in understanding aerosol diurnal variations, which can generally be classified into two categories: the diurnal cycle of ground-level air pollutants (Jia et al., 2018; Huszar et al., 2020; Shivkumar et al., 2022; Wang et al., 2021; Diya et al., 2024), and the diurnal variation of column-integrated aerosol optical properties (Reddy et al., 2015; Smirnov et al., 2002; Song et al., 2018). The vertical distribution of aerosols establishes a strong linkage between ground-level aerosol concentrations and column-integrated aerosol properties. It exhibits pronounced diurnal variability, driven by synoptic-scale systems and atmospheric boundary layer (ABL) evolution. Compared with the abundance of ground-level observations and column-integrated aerosol properties measurements, continuous, high-resolution observations of aerosol vertical distribution remain scarce. This observational imbalance limits our ability to connect surface aerosol variations with column-integrated optical properties through the intermediate vertical structure, particularly on diurnal timescales (Li et al., 2020; Cheng et al., 2020; Yorks et al., 2023; Bellini et al., 2025). Aerosols are primarily concentrated within the ABL; the diurnal cycle of the ABL constitutes the fundamental dynamical regime and dominant framework governing the diurnal evolution of aerosol vertical structure (Su et al., 2020b; Hara et al., 2022; Zhang et al., 2023b; Song et al., 2024). Local circulations, such as sea–land breezes and mountain–valley winds, drive diurnally reversing vertical transport, thereby governing aerosol layering, accumulation, and migration through modulation of vertical diffusion and transport processes throughout the day (Boselli et al., 2009; Zhang et al., 2023a). Inversion layers form a stable stratification structure whose diurnal evolution directly controls the intensity of atmospheric vertical exchange and the extent of aerosol trapping (Li et al., 2022; Liu et al., 2024; Parajuli et al., 2020), while turbulent mixing serves as the primary physical mechanism governing aerosol vertical transport and redistribution (Li et al., 2019; Noh et al., 2013). Meanwhile, diurnal variability in anthropogenic emissions intensity, as well as the altitude and strength of long-range transport, significantly influences aerosol vertical structure (Du et al., 2020; Cheng et al., 2020; Xiang et al., 2021; Yim and Huang, 2023). In addition, the interactions between aerosol and boundary layer, particularly the radiative effects of absorbing particles, can induce positive feedback mechanisms that alter stratification stability and suppress boundary layer development (Prasad et al., 2022; Su et al., 2020b), thereby modulating aerosol vertical structure. Although substantial progress has been made in understanding the diurnal variation of aerosol vertical distributions, important knowledge gaps remain. These gaps are particularly pronounced in arid and semi-arid regions with complex terrain, where high-resolution profile observations are scarce and the diurnal characteristics of boundary-layer aerosol vertical structure remain largely unexplored (Yorks et al., 2023; Parajuli et al., 2020). Consequently, the thermodynamic and dynamical mechanisms governing these variations, together with their regional air-quality and radiative impacts, remain poorly understood (Su et al., 2020b).

The Hexi Corridor is located adjacent to the northeastern margin of the Qinghai–Tibet Plateau and the surrounding deserts and Gobi regions. It serves as an ecological barrier in the arid and semi-arid regions of Northwest China. On the one hand, it strongly restricts the geographical expansion of deserts, forming the first line of defense against sand encroachment and desertification in inland Northwest China. On the other hand, it plays a critical role in protecting the scarce and valuable water resources of Northwest China, serving as a core lifeline for maintaining ecological balance in arid regions and ensuring water security for both human livelihoods and ecosystems. As the source region of several inland rivers, the Qilian Mountains within the Hexi Corridor act as a key regulator of regional water availability and ecosystem sustainability through orographic precipitation and glacial meltwater supply. Absorbing aerosols, such as dust and black carbon, when transported and deposited onto glaciers and snow cover in high-mountain regions, accelerate ablation by reducing surface albedo, thereby directly impacting water resource storage and security (Ramanathan et al., 2007; Sarangi et al., 2020; Hou et al., 2018). Additionally, aerosols significantly influence the microphysical processes and precipitation efficiency of mountainous clouds, potentially altering local precipitation patterns (Chen et al., 2011; Jian et al., 2025; Zhao et al., 2024). Therefore, conducting aerosol research in such regions is of great significance for environmental sustainability and ecological protection. In addition, significant efforts have been made in recent years to strengthen the construction of a regional three-dimensional observation network over the Hexi Corridor region (Huang et al., 2024; Yang et al., 2025); however, the diurnal cycle of aerosol vertical distribution and its regional impacts have not yet received sufficient attention.

In this study, the phenomenon of elevated aerosol layers embedded within the daytime mixed layer were focused, which has hardly been reported before, to investigate their identification, occurrence, vertical characteristics, associated meteorological conditions, and potential air-quality and shortwave radiative effects based on two intensive observation periods conducted in 2010 at Minqin and in 2012 at Dunhuang over the Hexi Corridor, an ecologically sensitive arid and semi-arid complex-terrain region. Section 2 introduces the study sites and methodologies. Section 3 analyses the characteristics of diurnal variation in aerosol vertical distribution, explores the underlying mechanisms, and evaluates the associated radiative and environmental effects. Finally, the conclusions are presented in Sect. 4.

## 2 Data and methods

### 2.1 Field campaigns

This study utilises data from intensive field observations conducted using the mobile facilities of the Semi-Arid Climate and Environment Observatory of Lanzhou University (SACOL) (Fig. 1) at Minqin (38.607° N, 102.959° E, 1373 m a.s.l.) from April to June 2010 and at Dunhuang (40.492° N, 94.955° E, 1061 m a.s.l.) from April to June 2012 in the Hexi Corridor region. The mobile facilities were equipped with a suite of instruments to measure key atmospheric parameters, including atmospheric radiation, aerosol scattering and absorption coefficients, aerosol optical depth, mass concentration, and aerosol vertical distribution. Dunhuang is located at the westernmost end of the Hexi Corridor, adjacent to the Kumtag Desert to the west, approximately 450 km downwind of the Taklimakan Desert, bordering the Badain Jaran Desert to the east, and close to the Qilian Mountains to the south. Owing to its unique geographical location, distinctive underlying surface characteristics, extreme aridity, and strong prevailing winds, dust storms frequently occur in this region during spring. The observation site was located approximately 45 km northeast of Dunhuang City and was surrounded by farmland, Gobi Desert, and saline–alkali land. Minqin is located in the northeastern part of the Hexi Corridor, at the convergence zone of the Badain Jaran and Tengger Deserts, and is close to the Qilian Mountains to the southwest, making it highly susceptible to aeolian processes. The region is characterised by a temperate continental hyperarid climate. Dust events also occur frequently during springtime. The observation site was surrounded by sand dunes interspersed with small patches of farmland, representing a typical desert–oasis transition zone (Zhou et al., 2018).

### 2.2 Observation Instruments

#### 2.2.1 Micro-Pulse Lidar (MPL)

The micro-pulse lidar (MPL-4B; manufactured by Sigma Space Corporation) is a safe, compact, and maintenance-free system with a wavelength of 527 nm, a temporal resolution of 1 min, a spatial resolution of 30 m, an emission energy of 6–8 µJ, a pulse repetition frequency of 2500 Hz and a blind zone of 600 m. MPL observations are corrected and preprocessed using the algorithm proposed in previous studies (Xie et al., 2017; Zhou et al., 2018). Subsequently, aerosol optical properties, including the extinction coefficient, backscattering coefficient, particle depolarization ratio, cloud top and base heights, and cloud thermodynamic phase, are retrieved.

To identify elevated aerosol layers in this study, the following discrimination procedure was adopted: observations between 13:00 and 21:00 Beijing Time (the period of frequent occurrence of elevated aerosol layers) were selected for analysis; consistent with previous dust aerosol identification criteria, a depolarization ratio greater than 0.20 was used as the threshold for identifying dust aerosols (Zhou et al., 2018, 2021). For both sites, if the proportion of observations identified as dust aerosols exceeded 50 % on a given day, that day was classified as a dust event and subsequently excluded from further analysis. For the remaining non-dust observations, elevated aerosol layers were identified based on the spatiotemporal continuity of the positive-gradient structure in the aerosol extinction coefficient profiles. In this study, a "continuous positive gradient" refers to a fitted aerosol extinction coefficient profile that increases persistently with height from the first valid value above the lidar blind zone to the altitude of the aerosol-layer peak, with this increasing structure required to be continuous in both height and time. If the proportion of observations satisfying this continuous positive-gradient criterion within this time window exceeded 20 %, an elevated aerosol layer was considered to be present. The selection of the 50 % and 20 % thresholds was based on the stability of event classification. Specifically, different threshold combinations were systematically evaluated, and the variability of the resulting classifications was analysed, as shown in Fig. S1 in the Supplement. The optimal combination – defined as that which minimized classification fluctuations and maximized consistency – was ultimately selected as the determination criterion.

Additionally, to estimate the Extinction-derived $PM_{10}$-equivalent mass concentration of elevated aerosol layers at higher altitudes, a site-specific empirical relationship was established between ground-level $PM_{10}$ observations and the aerosol extinction coefficient in the lowest two bins of vertical profiles (near 600 m). The 1 min MPL-derived extinction coefficients were matched with the 5 min ground-level $PM_{10}$ observations at the corresponding observation times during the intensive observation period. As shown in Fig. S2 in the Supplement, a significant positive correlation was found

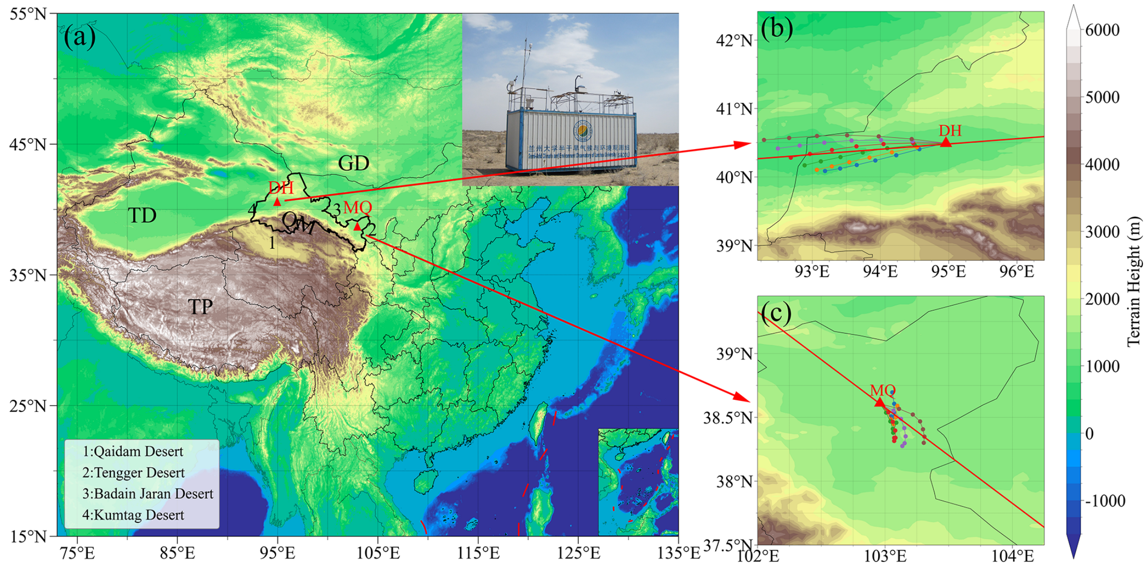


**Figure 1.** Observation locations of Dunhuang (DH) and Minqin (MQ), their surrounding areas, and photographs of the mobile facilities. HYSPLIT backward trajectories are shown, and the red lines in the right panel represent the selected cases in Dunhuang and Minqin.

between $PM_{10}$ mass concentration and the aerosol extinction coefficient ($\alpha$) ($r = 0.80$, $n = 4357$). A linear regression based on these collocated observations yielded the following empirical equation:

$$PM_{10} = 914.65 \times \alpha - 56.26 \quad (1)$$

where $\alpha$ is the aerosol extinction coefficient in $km^{-1}$, and $PM_{10}$ represents the $PM_{10}$-equivalent mass concentration estimated from aerosol extinction coefficients using an empirical relationship, expressed in $\mu g\, m^{-3}$.

### 2.2.2 Other Data and Tools

The aerosol optical depth (AOD) and Ångström exponent (AE) used in this study were retrieved from a Cimel CE-318 sun photometer, a passive remote-sensing instrument manufactured by CIMEL (France), designed to measure both direct solar and diffuse sky radiation. This instrument serves as the standard platform within the AERONET (Aerosol Robotic Network) observation network (Holben et al., 1998). The CE-318 is equipped with multiple spectral channels (e.g. 440, 670, 870, 936, and 1020 nm) and performs automated sun-tracking and sky-scanning measurements at 15 min intervals. Single-scattering albedo (SSA) and the asymmetry factor (ASY) were also retrieved from the AERONET database (Marsli et al., 2025). The SSA and ASY represent statistically averaged aerosol optical properties derived from Level 1.5 AERONET products based on observations at the Dunhuang and Minqin sites.

Ground-level meteorological parameters, including air temperature, relative humidity, air pressure, wind speed, and wind direction, were measured using an automatic meteorological station (model WXT520; Vaisala, Vantaa, Finland). The instrument was mounted on top of a mobile platform at an approximate height of 4 m above ground level. Raw data averaged at 1 min intervals were used in this study.

$PM_{10}$ mass concentration was continuously monitored using an ambient particulate monitor with a resolution of $0.1\, \mu g\, m^{-3}$. This instrument operates based on the principle of a tapered element oscillating microbalance (TEOM; model RP1400a, Rupprecht and Patashnick Company) with a flow rate of $16.7\, L\, min^{-1}$ (Patashnick and Rupprecht, 1991). In this study, instances in which negative $PM_{10}$ concentration values occurred due to heating of the sampling stream (50 °C) and the partial loss of volatile and semi-volatile aerosol compounds were excluded. These negative values accounted for less than 1 % of the total dataset (Bi et al., 2017; Zhou et al., 2018).

Meteorological conditions and the formation mechanisms of elevated aerosol layers were characterised and analysed using the ERA5 reanalysis dataset (available at https://cds.climate.copernicus.eu/, last access: 15 October 2025), a high-resolution global atmospheric reanalysis product developed by the European Centre for Medium-Range Weather Forecasts (ECMWF). This comprehensive dataset, spanning from 1979 to the present, with an hourly temporal resolution (1 h) and a spatial resolution of $0.25° \times 0.25°$, provides 37 vertical pressure levels ranging from 1000 to 1 hPa and includes key meteorological parameters such as temperature, pressure, wind fields, relative humidity, and cloud cover (Nogueira, 2020; Albergel et al., 2018).

To trace air mass source regions, the Hybrid Single-Particle Lagrangian Integrated Trajectory (HYSPLIT) model was employed. This modelling system, developed by the Air Resources Laboratory (ARL) of the National Oceanic and Atmospheric Administration (NOAA), is widely used to simulate the transport and dispersion of aerosols, gases, and other atmospheric constituents. It integrates the advantages of both Lagrangian particle models and Eulerian grid-based models, thereby enabling the simulation of atmospheric transport processes across a wide range of spatial scales, from local to global (Stein et al., 2016).

To quantify the radiative effects of elevated aerosol layers, this study employed the Santa Barbara DISORT Atmospheric Radiative Transfer (SBDART) model, which is grounded in well-established radiative transfer theory and is widely used in remote sensing applications and atmospheric energy budget analyses (Ricchiazzi et al., 1998). In this study, the model input parameters were constrained using multiple observational datasets to improve the accuracy of radiative forcing simulations. These inputs include shortwave (0.3–2.8 µm) radiative flux, surface albedo, and site location data obtained from an automatic meteorological station. Additional aerosol optical properties, including aerosol optical depth and Ångström exponent, along with water vapour parameters, were retrieved from a CE-318 sun photometer. Aerosol and atmospheric vertical profiles, including air density, specific humidity, temperature, and ozone, were derived from lidar observations and reanalysis datasets (ERA5 and MERRA2), with the latter additionally providing hourly atmospheric profiles. Furthermore, total column ozone was retrieved from the Ozone Monitoring Instrument. These dynamically constrained inputs resulted in excellent model performance, as evidenced by the high coefficients of determination between simulated and observed radiation components. Specifically, the coefficients of determination ($R^2$) between simulated and observed direct and diffuse radiation were 0.999 and 0.982, respectively (not shown here), thereby confirming the robustness of the model configuration. (Li et al., 2025)

Here, the shortwave radiative forcing (SRF) and shortwave heating rate are calculated under clear-sky conditions (Jangid et al., 2024). Following the formulations of Li et al. (2025), Eqs. (2)–(6) can be expressed as follows:

$$\Delta F = F\downarrow - F\uparrow \quad (2)$$

where $\Delta F$ denotes the net downward radiative flux.

$$\mathrm{SRF(TOA)} = \Delta F^{\mathrm{aerosol}}(\mathrm{TOA}) - \Delta F^{\mathrm{no}}(\mathrm{TOA}) \quad (3)$$

$$\mathrm{SRF(SFC)} = \Delta F^{\mathrm{aerosol}}(\mathrm{SFC}) - \Delta F^{\mathrm{no}}(\mathrm{SFC}) \quad (4)$$

$$\mathrm{SRF(ATM)} = \mathrm{SRF(TOA)} - \mathrm{SRF(SFC)} \quad (5)$$

TOA, SFC, and ATM denote the top of the atmosphere, the surface, and the atmospheric column, respectively. The labels “aerosol” and “no” indicate conditions with and without aerosols, respectively.

$$\mathrm{ASHR}(z) = \mathrm{SHR}(z)^{\mathrm{aerosol}} - \mathrm{SHR}(z)^{\mathrm{no}} \quad (6)$$

where $\mathrm{ASHR}(z)$ denotes the aerosol shortwave heating rate at height $z$.

## 3 Results and discussion

### 3.1 Overview of field observations

First, the meteorological background during both intensive observation periods is shown in Fig. 2. It can be seen that both sites are influenced by the westerlies at the 500 hPa level. At the 700 and 850 hPa levels, the influence of complex topography becomes evident. The wind direction at both sites aligns with the orientation of the Qilian Mountains, with airflow predominantly from northwest to southeast. Areas surrounding the Qilian Mountains and the Hexi Corridor exhibit relatively high potential temperatures, suggesting enhanced thermal buoyancy. Under weakly stable or potentially unstable stratification, such thermodynamic conditions can favour the development of vertical motion (Houze, 2004; Li et al., 2017). At the Dunhuang site, wind speeds are relatively high, generally exhibiting a north-to-south flow pattern. In contrast, wind speeds at the Minqin site are lower, and the low-level flow field near the site shows weak convergence that may favour ascent. Overall, the mean meteorological fields suggest that parts of the Hexi Corridor experienced conditions favourable for upward motion and aerosol transport during the campaigns.

The complex mountainous terrain also generates distinct patterns in the local distribution of wind speed and direction. Concurrently, the extensive surrounding desert surfaces serve as major aerosol sources, profoundly influencing local aerosol composition and speciation. As shown in Fig. 3, northeasterly and southwesterly winds prevail at the Dunhuang site, with an average wind speed of 3.5 $\mathrm{m\,s^{-1}}$. Aerosols are likely derived mainly from dust originating from the Gobi Desert and sandy areas surrounding the observation site, as well as from the Kumtag Desert to the southwest (Luo et al., 2022). At the Minqin site, southeasterly winds dominate, with an average wind speed of 3.2 $\mathrm{m\,s^{-1}}$. Aerosols are likely primarily derived from dust originating from the Tengger Desert to the southeast or the Badain Jaran Desert to the northwest (Yang et al., 2024). The prevailing wind directions of both sites not only exhibit higher frequencies of occurrence but are also associated with relatively higher wind speeds, which are closely related to wind channelling effects induced by topographic undulations (Dang et al., 2024).

The evolution of aerosol vertical distribution and column properties over Dunhuang is presented in Fig. 4. In Fig. 4a and b, high normalised relative backscatter and high depolarization ratios indicate elevated dust aerosol loading, including dust events (Zhou et al., 2021, 2024). Dust events frequently occurred before 4 May. Thereafter, although dust events still occurred, their intensity and duration were significantly reduced. Instead, more distinct diurnal variations in aerosol vertical distribution are observed. These vertical distributions exhibit high normalised relative backscatter but a broader range of depolarization ratios, indicating that not all

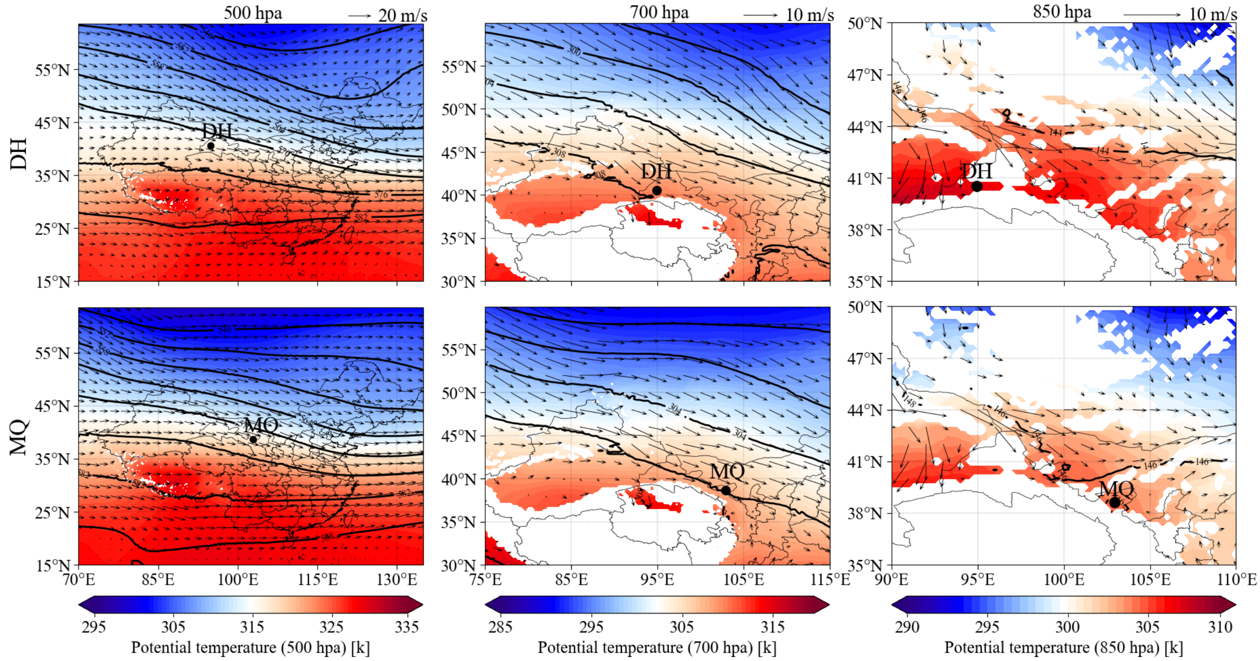


**Figure 2.** Mean meteorological fields during the two intensive observation periods (Dunhuang: 1 April–10 June 2012; Minqin: 21 April–15 June 2010), with geopotential height contours. The white regions indicate elevated mountainous terrain.

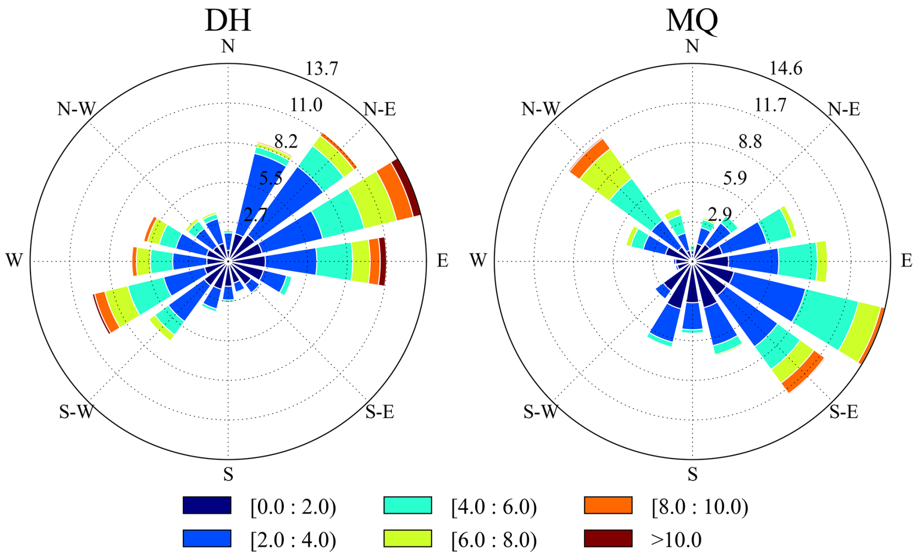


**Figure 3.** Surface wind speed and wind direction during the intensive observation periods at Dunhuang from 1 April to 10 June 2012 (left) and Minqin from 21 April to 15 June 2010 (right).

observations correspond to dust particles. The maximum normalised relative backscatter is located at approximately 1 km, indicating the presence of elevated aerosol layers. According to the method described in Sect. 2.2.1, the occurrence frequency of elevated aerosol layers is approximately 82 % during the experimental period, excluding dust events. As shown in Fig. 4c, most of these events occurred after 10 May. Owing to the limited availability of CE-318 observations during the experiment, aerosol column properties were derived by column-integrating the aerosol extinction coefficient retrieved from lidar to calculate AOD, following the approach used in our previous study (Zhou et al., 2021). The correlation coefficient between the two AOD datasets is 0.86, with a root-mean-square error of 0.18. This indicates the reliability of AOD retrieved from lidar in the absence of CE-318 observations. AOD values during elevated aerosol layer episodes were considerably lower than those during dust events, and the variability in AOD during each episode remained relatively consistent. To a certain extent, the depolarization ratio can characterise the coarse- and fine-mode particle fractions. For example, on 5 and 11 April, lower depolarization ratios correspond to higher Ångström exponent (AE) values, indicating that the elevated aerosol layers contain a larger fraction of fine-mode particles (Huang et al., 2025). Similar patterns are observed on 14 May and 7–8 June. However, relatively high depolarization ratios observed on 18 and 23 May, indicate the presence of mixed aerosol types containing dust components.

Similarly, Fig. 5 provides an overview of aerosol evolution over Minqin. A notable contrast is observed compared with Dunhuang, despite the consistency of observation season. High dust loading was also observed at Minqin; however, dust events were less intense but more frequent and temporally dispersed than those at Dunhuang, occurring intermittently throughout the experiment, with the highest frequency in May. In contrast to the lower values observed at Dunhuang, depolarization ratios remained consistently high at Minqin. This indicates that concentrations of coarse-mode particles (e.g., dust aerosols) were comparatively higher at Minqin during the observation period. For elevated aerosol layers (excluding dust days), the occurrence frequency at Minqin was only 44 %, with such events primarily concentrated in June (Fig. 5c). Moreover, the overall height of elevated aerosol layers at Minqin was lower than that at Dunhuang, and their intensity was also weaker. The correlation coefficient between AOD values retrieved by lidar and CE-318 was 0.70, with a root-mean-square error of 0.06. Notably, the AE was relatively high in June, when elevated aerosol layer events were frequent. In particular, the mean AE reached 0.6 during elevated aerosol layer events, indicating the dominance of fine-mode aerosols during this period.

## 3.2 Diurnal variation

To provide a more intuitive representation of the diurnal variations in aerosol vertical structure at the two sites, hourly averaged extinction coefficient profiles at specific times during the experimental periods are presented in Fig. 6. Within the vertical range of 0.6–2 km a.g.l. at Dunhuang, the aerosol extinction coefficient exhibited a weak decreasing trend from 22:00 to 12:00 BJT the following day. However, from 14:00 to 20:00, a distinct nose-shaped structure appeared, with a peak near 1.26 km a.g.l., reaching a maximum value of approximately 0.27 $km^{-1}$ at around 18:00 BJT. Even when dust-influenced profiles were included in the averaging, a pronounced nose-shaped vertical distribution pattern was still observed. This indicates that elevated aerosol layers occurred more frequently and with greater intensity during the afternoon period. In contrast, the low frequency of elevated aerosol layers, coupled with the influence of dust events, resulted in the mean aerosol extinction coefficient profile at Minqin not exhibiting a distinct nose-shaped structure. Nevertheless, diurnal variation characteristics were still evident: the extinction coefficient was significantly higher from 10:00 to 18:00 than at night below 2 km a.g.l., particularly between 10:00 and 12:00, when the extinction coefficient in the lower altitude exceeded 0.4 $km^{-1}$, indicating a significant increase in aerosol loading within 2 km. The depolarization ratio in the lower altitude exhibited a similar trend, remaining mostly below 0.3 at both sites, with slightly higher values at Minqin. This earlier occurrence of the peak at Minqin may be partly related to geographical differences between the two regions, including the longitudinal difference and the resulting local-time effect, which can influence the timing of boundary layer development. Overall, these averaged profiles indicate that daytime boundary layer evolution plays an important role in regulating the vertical redistribution of aerosols, providing the basis for the representative case analyses discussed below.

Furthermore, two representative cases at both sites are presented to illustrate the diurnal variation of aerosol vertical distribution and the associated thermal and dynamical factors, particularly during periods when elevated aerosol layers occur. As shown in Fig. 7a and b, except during the period of full daytime boundary layer development (approximately 14:00–20:00 BJT), the aerosol extinction coefficient at Dunhuang was relatively low (mean: 0.14 $km^{-1}$), while the depolarization ratio remained high (mean: 0.21), indicating relatively low aerosol loading with a substantial dust contribution. When elevated aerosol layers were present from 15:00 to 20:00 BJT, a high aerosol extinction coefficient ($\sim 0.27\,km^{-1}$) was observed at approximately 1 km, while the depolarization ratio decreased to 0.17, suggesting an increased contribution of non-spherical dust mixed with finer or less-depolarizing particles. During this period, AOD at 440 nm ranged between 0.15 and 0.26, and AE at 440–870 nm ranged between 0.3 and 0.5. Meanwhile, SSA exhibited a distinct wavelength dependence characteristic of dust-dominated aerosols (Dubovik et al., 2002; Tutsak and Koçak, 2020), with lower values at 440 nm and higher values at longer wavelengths (not shown here). In addition, the weakened potential temperature gradient within the daytime boundary layer indicates reduced static stability and enhanced vertical mixing, which favoured the upward transport of aerosols from the lower atmosphere. The stable stratification near the boundary layer top further limited upward dispersion, thereby promoting aerosol accumulation and the formation of the elevated aerosol layer. As illustrated in Fig. 7c, the prevalence of southwesterly winds during elevated aerosol layer episodes suggests that aerosols were likely associated with desert source regions to the southwest. This is consistent with the backward trajectories of air masses presented in Fig. 1. In Fig. 7d, elevated aerosol layer episodes were accompanied by a rapid increase in surface temperature, reaching the daily maximum, while pressure and relative humidity decreased sharply. These concurrent

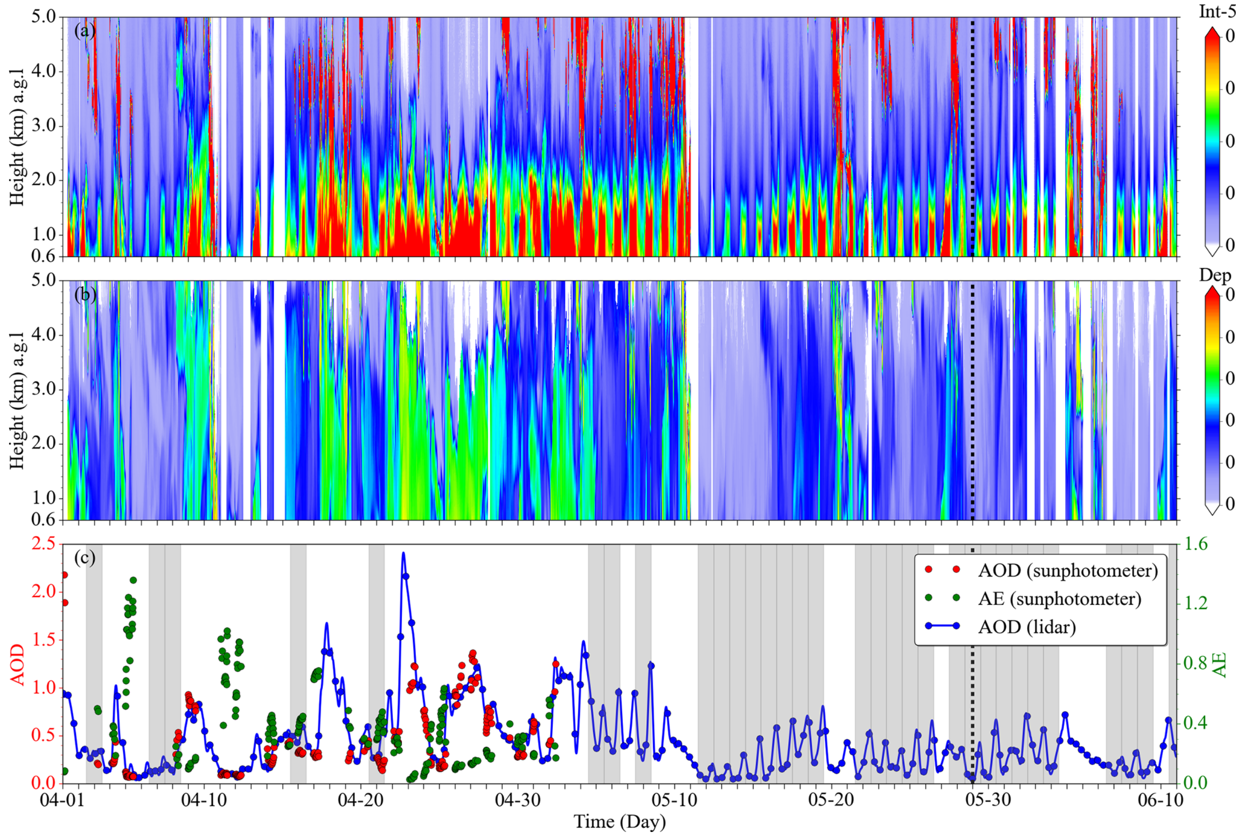


**Figure 4.** Time series of observations obtained from a micro-pulse lidar (MPL) and a sun photometer during the intensive observation period at Dunhuang in 2012. Time–height cross-sections of **(a)** normalised relative backscatter (NRB) and **(b)** linear volume depolarization ratio (Dep) derived from MPL observations. **(c)** Time series of aerosol optical depth (AOD) retrieved from AERONET at 500 nm (red dots) and from MPL at 527 nm, along with the Ångström exponent (AE) at 440–870 nm (green dots). All identified elevated aerosol layers are indicated by shaded regions, and the representative case selected for detailed discussion is highlighted with black dashed lines.

changes in aerosol vertical structure and near-surface meteorological conditions indicate that daytime thermodynamic processes played an important role in the formation of the elevated aerosol layer.

Along the HYSPLIT backward trajectories, vertical cross-sections of relative humidity and potential temperature reveal that the elevated transport and accumulation of aerosols over the Dunhuang region were closely associated with daytime thermodynamic evolution within the boundary layer. For the case shown in Fig. 8, three representative time points were selected to examine the evolution of the thermodynamic structure, representing the pre-event (10:00 BJT), during-event (16:00 BJT) and post-event (22:00 BJT) stages of the elevated aerosol layer episode. During these three stages, relative humidity in the lower atmosphere remained approximately 10 % (Fig. 8a–c), consistent with the surface observations shown in Fig. 7d. Such dry lower-atmospheric conditions favoured enhanced daytime sensible heating, while the strong surface thermal contrasts between the low-altitude desert areas and the surrounding terrain further promoted thermally driven vertical motion and the upward transport of aerosols (Mazza and Chen, 2025; Pal et al., 2025; Wen et al., 2025). To better characterise the elevated aerosol layer, the meteorological field near 650 hPa is analysed (Fig. 8d–f). At this level, westerly winds persisted, and the geopotential height field showed a relatively smooth north–south gradient. No prominent synoptic disturbance or strong convective system directly affected the Dunhuang region during this event. These characteristics indicate that the upper part of the boundary layer environment was relatively stable. Under such meteorological conditions, stable stratification can effectively suppress vertical air motion and limit the further upward dispersion of aerosols (Haeffelin et al., 2024; Hu et al., 2024; Zhong et al., 2018).

Before the elevated aerosol layer episode, although the potential temperature at 800 hPa in the vicinity of the Dunhuang region remained relatively low, a thermal gradient had already developed between the desert areas to the west of the site and those to the east (Fig. 8g). In addition, the potential temperature gradient over the Dunhuang region was large, with gently sloping isentropic surfaces indicating stable stratification, which impeded the upward transport of aerosols

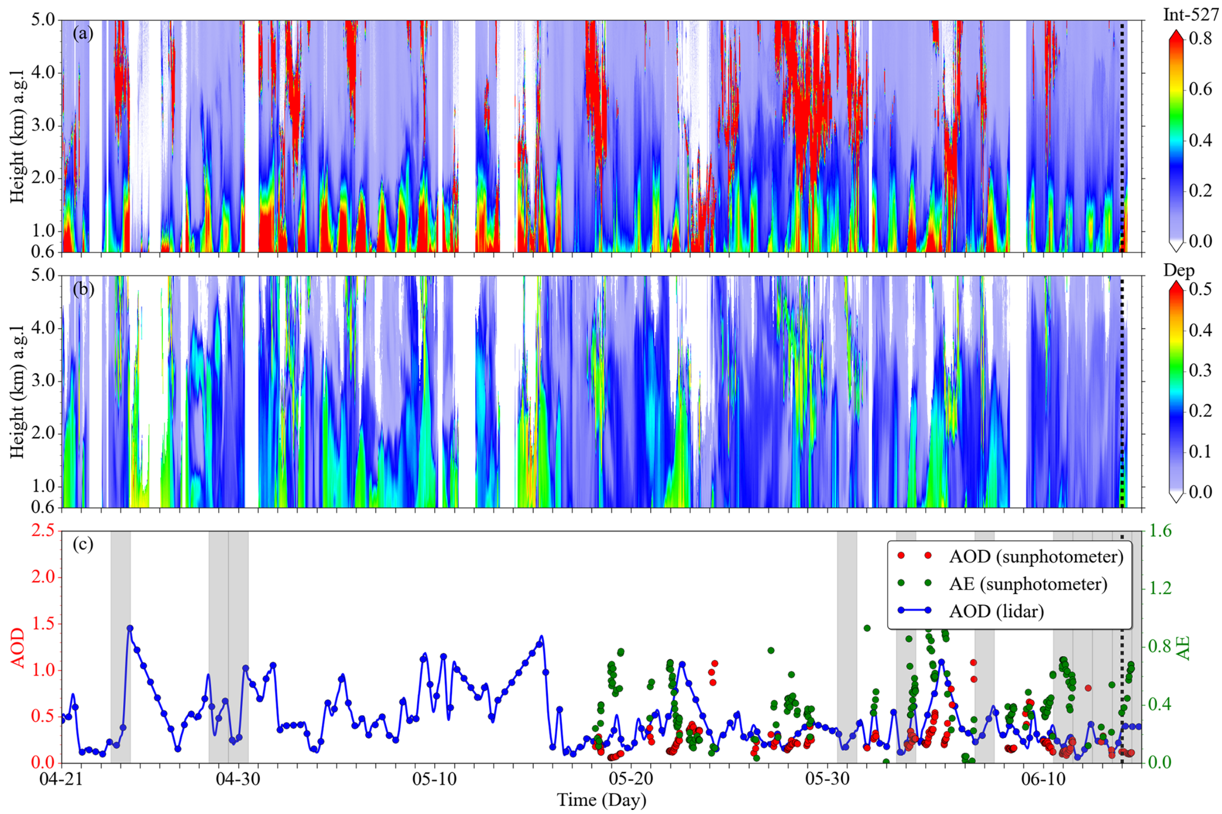


**Figure 5.** Time series of observations obtained from a micro-pulse lidar (MPL) and a sun photometer during the intensive observation period at Minqin in 2010. Time–height cross-sections of **(a)** normalised relative backscatter (NRB) and **(b)** linear volume depolarization ratio (Dep) derived from MPL observations. **(c)** Time series of aerosol optical depth (AOD) retrieved from AERONET at 500 nm (red dots) and from MPL at 527 nm, along with the Ångström exponent (AE) at 440–870 nm (green dots). All identified elevated aerosol layers are indicated by shaded regions, and the representative case selected for detailed discussion is highlighted with black dashed lines.

and confined them to the lower atmosphere (Li et al., 2021b). As time progressed, intense daytime solar radiation strongly heated the surface in low-altitude areas, where the low heat capacity of the underlying surface allowed rapid warming. This caused substantial increases in surface potential temperature, resulting in upward-bulging isentropic surfaces and a sharp decrease in the potential temperature gradient. Meanwhile, ascending airflows developed under the influence of thermal buoyancy (De Wekker et al., 2018), facilitating the upward transport of aerosols in the lower atmosphere. During the formation of the elevated aerosol layer, the lower atmosphere transitioned from stable to unstable or weakly stable stratification, with enhanced vertical mixing observed at mean heights of approximately 0.3–1.3 km a.g.l. (Fig. 8b), although the thickness of this layer varied considerably (Jin et al., 2022). This thermodynamic structure favoured the upward transport of aerosols. Upon reaching the overlying stable stratification, the lifted air parcels encountered negative buoyancy and tended toward hydrostatic equilibrium (Serafin et al., 2018), thereby inhibiting further vertical motion. As a result, aerosols accumulated within the altitude range of 0.6–2 km a.g.l. and tended to concentrate near the base of the stable stratification. This finding is consistent with those reported in other regions (Su et al., 2020a; Meng et al., 2025). Following the elevated aerosol layer episode, surface cooling occurred as solar heating diminished. Despite the persistence of relatively high potential temperatures at this moment, isentropic surfaces gradually flattened and atmospheric stratification progressively returned to a stable state (Fig. 8c). In combination with relatively strong wind speeds within this altitude layer (Fig. 8i), these meteorological conditions facilitated the rapid dissipation of the elevated aerosol layer.

Furthermore, as illustrated in Fig. 8g–i, terrain-induced local circulations near the Qilian Mountains may modulate the horizontal diffusion and transport of elevated aerosol layers. During daytime, differential heating between low-altitude desert areas and the surrounding mountainous terrain can induce upslope or valley winds, favouring aerosol transport from low-altitude regions toward the mountains under suitable background wind conditions (Cacciani et al., 2018; Serafin et al., 2018). However, for the case illustrated in Fig. 8, southwesterly winds prevailed during the formation of the elevated aerosol layer, indicating that the transport pathway was not directed toward the Qilian Mountains. There-

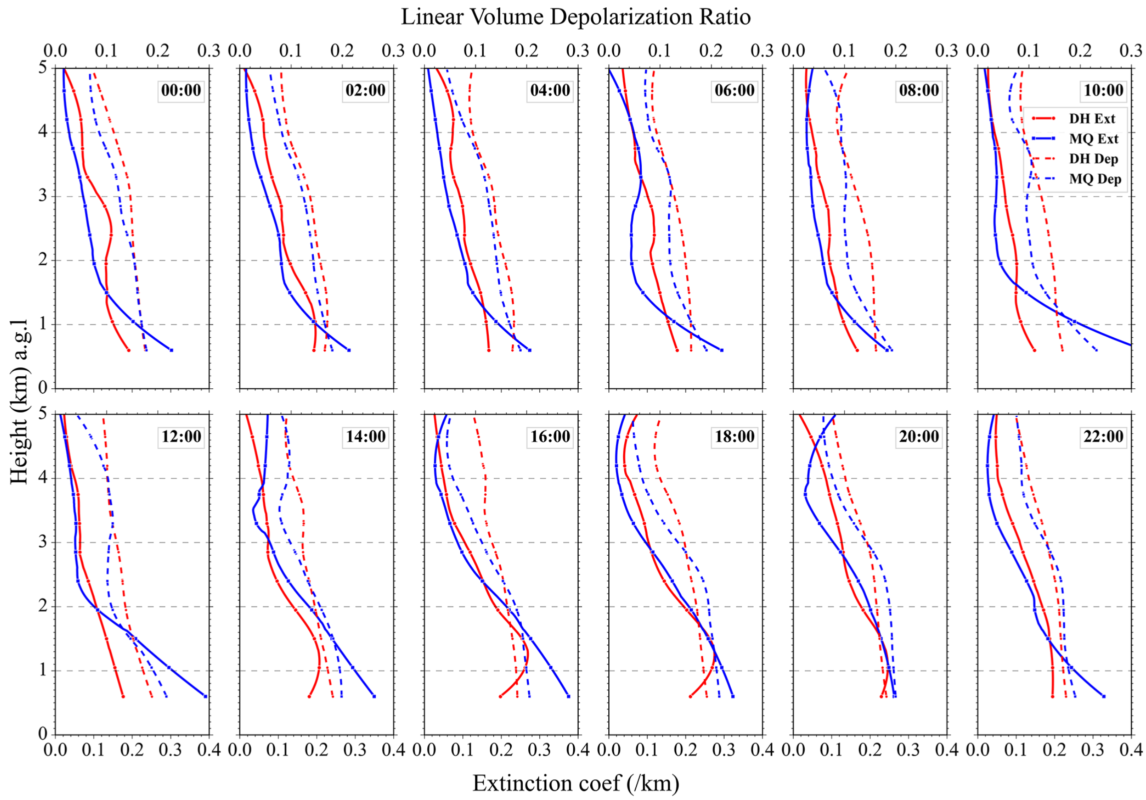


**Figure 6.** Hourly averaged vertical profiles of aerosol extinction coefficient (solid lines) and linear volume depolarization ratio (dashed lines) during the experimental periods at Dunhuang (red lines) and Minqin (blue lines).

fore, the influence of this particular EAL event on the Qilian Mountains was likely limited. This case-specific result does not exclude the possibility of regional impacts under other wind regimes. Nevertheless, as shown in Fig. 3, northeasterly winds also occurred frequently at the Dunhuang site. Under such conditions, daytime mountain–valley circulations may facilitate the transport of elevated aerosol layers from the Dunhuang region toward the Qilian Mountains. This process may contribute to localized pollution and has potential implications for snow/glacier environments in the Qilian Mountains (Hou et al., 2018).

Similar to the Dunhuang case shown in Fig. 7, a distinct elevated aerosol layer was observed at Minqin on 14 June 2010 (Fig. 9). Consistent with the observations at Dunhuang, the average aerosol extinction coefficient at Minqin remained relatively low ($\sim 0.08\,\mathrm{km}^{-1}$) for most of the observation period, except during the fully developed boundary layer stage (14:00–20:00 BJT), when it increased significantly to $0.23\,\mathrm{km}^{-1}$. However, the depolarization ratio at Minqin showed minimal variation throughout the observation period and remained low, with a value of approximately 0.09. This indicates that the elevated aerosol layer was primarily composed of spherical or weakly depolarizing particles, suggesting a larger contribution from fine-mode and/or anthropogenic aerosols than in the Dunhuang case. Based on the optical properties, during the elevated aerosol layer episode, AOD at 440 nm ranged from 0.08 to 0.14, and AE at 440–870 nm ranged from 0.65 to 0.75. In parallel, SSA exhibited a spectral pattern more consistent with fine-mode and anthropogenic aerosol contributions than with dust-dominated aerosols (Dubovik et al., 2002; Tutsak and Koçak, 2020): values at all four wavelengths (440, 675, 870, and 1020 nm) were comparable (0.86–0.92), with no pronounced gradient between short and long wavelengths (not shown here). Together with the low depolarization ratio and relatively higher AE, this SSA feature suggests that the Minqin elevated aerosol layer was more strongly influenced by fine-mode and anthropogenic aerosols than the Dunhuang case. Similar to Fig. 7, the case presented here represents only one example and does not imply that elevated aerosol layers at both sites are dominated by a single aerosol type. Combined with Figs. 4 and 5, it can be observed that both dust-influenced and fine-mode/anthropogenic-aerosol-influenced elevated layers occurred at both sites during the experimental periods, with differences likely arising from variations in dust aerosol content. Although not exclusively dominated by a single type, certain aerosol types exhibit higher occurrence frequencies and greater representativeness in each region. Compared with the Dunhuang case, the Minqin case therefore provides a contrasting example in terms

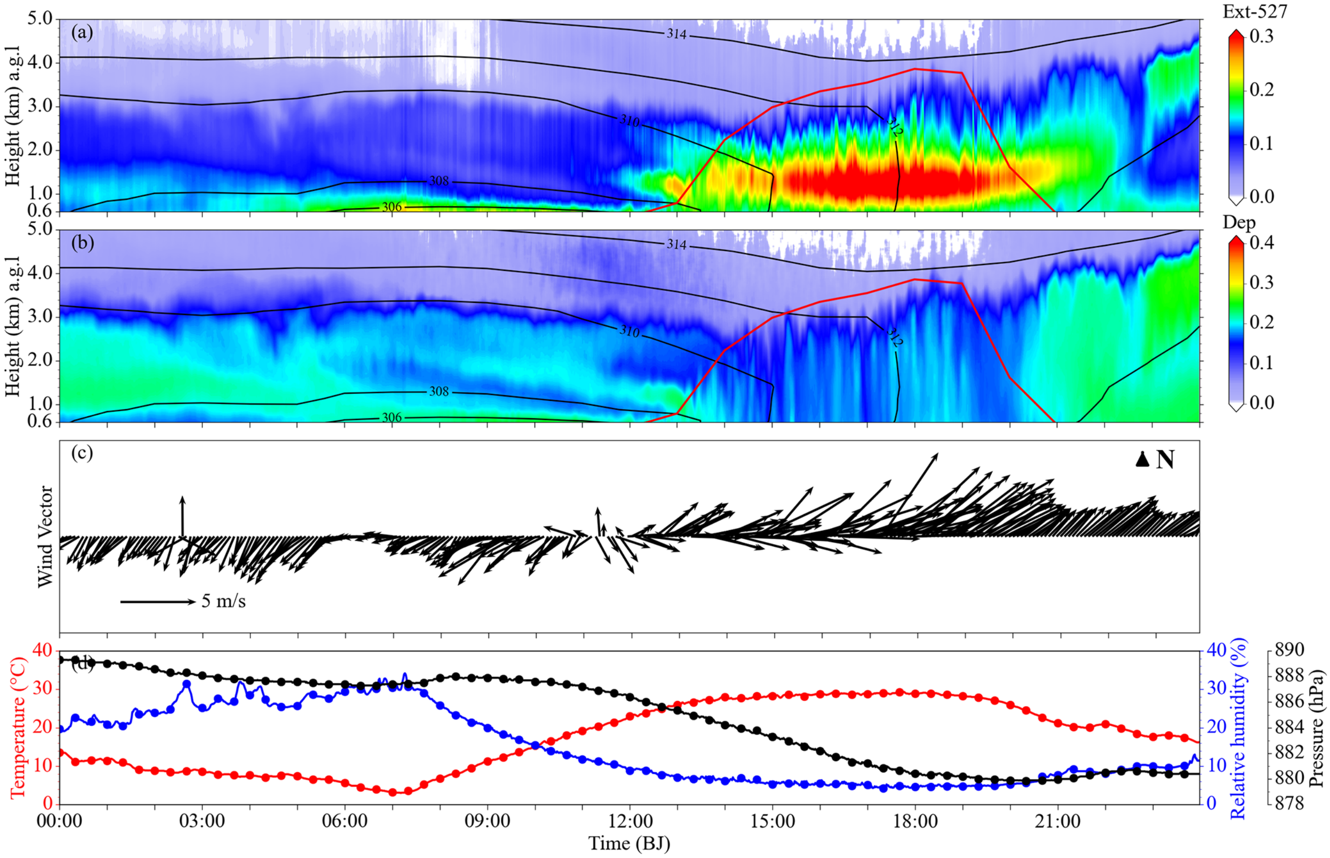


**Figure 7.** Time series of aerosol vertical distribution and meteorological parameters at Dunhuang on 21 April 2012. **(a)** Time–height cross-sections of aerosol extinction coefficient and **(b)** depolarization ratio derived from MPL lidar, with potential temperature contours (black lines) and boundary layer height (red lines) from ERA5. **(c)** Wind vectors measured by an automatic meteorological station (model WXT520), and **(d)** temperature, relative humidity, and pressure.

of aerosol optical properties, while showing a broadly similar daytime thermodynamic evolution. The weakened potential temperature gradient within the daytime boundary layer indicates reduced static stability and enhanced vertical mixing, favouring the upward transport of aerosols. As shown in Fig. 9c, easterly winds prevailed during the aerosol layer episode. This transport pathway is consistent with the backward trajectories of air masses presented in Fig. 1. A similar pattern of the diurnal variations in temperature, humidity, and pressure is observed in Fig. 9d, suggesting that daytime thermodynamic processes also contributed to the formation of the elevated aerosol layer at Minqin. Overall, the Minqin case supports the common uplift–accumulation mechanism identified at Dunhuang, while highlighting site-dependent differences in aerosol optical characteristics under the broadly similar modulation of mountain–valley circulations.

Consistent with the approach adopted for the Dunhuang thermodynamic analysis in Fig. 8, three time points were selected to represent the evolution of the thermodynamic structure, corresponding to the pre-event (09:00 BJT), during-event (16:00 BJT) and post-event (23:00 BJT) stages of the elevated aerosol layer episode in Fig. 10. This selection of time points is based on the earlier initiation and later dissipation of the elevated aerosol layer in the Fig. 9 case compared with that in Fig. 7. In general, elevated aerosol layers at Minqin were also associated with daytime thermal forcing, upward aerosol transport, and terrain-induced circulation, suggesting a broadly similar thermodynamic coupling mechanism to that identified at Dunhuang. In contrast to Dunhuang, a pronounced abrupt change in relative humidity occurred at the upper boundary of the unstable stratification, with a larger vertical extent and nearly constant height, where a persistent high-relative-humidity zone was present (Fig. 10a–c). This feature indicates that the upper boundary of the unstable layer at Minqin was closely associated with a humid and relatively stable layer. Rather than directly implying that water vapour itself inhibited aerosol uplift, the coexistence of enhanced relative humidity and stable stratification suggests that this layer likely acted as a cap, limiting further upward dispersion of aerosols (Zhong et al., 2018; Wang et al., 2020).

Analysis of the corresponding height layer at the 600 hPa level (Fig. 10d–f) shows that, before the elevated aerosol

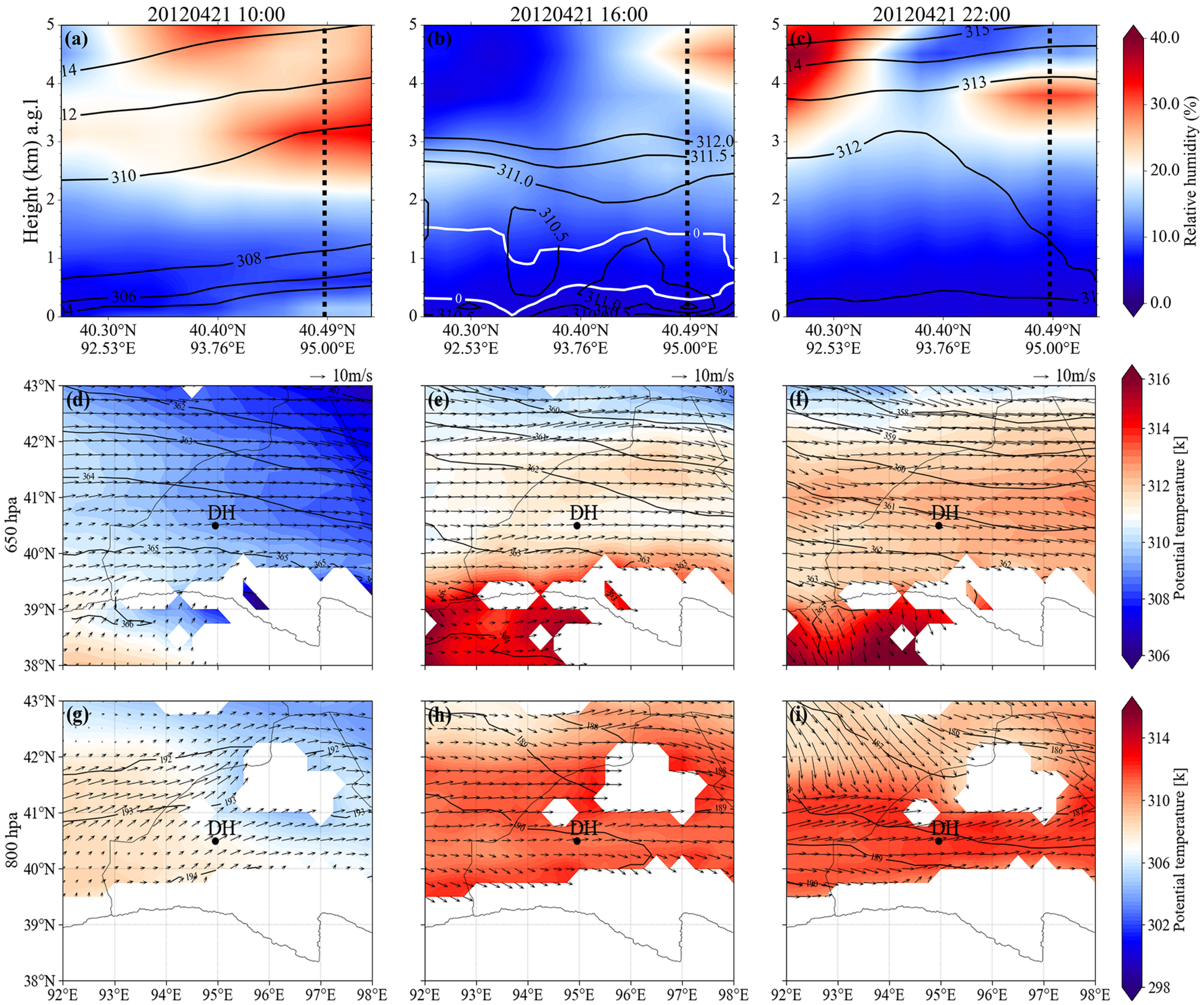


**Figure 8.** Thermal and dynamical fields at Dunhuang on 21 April 2012. **(a–c)** Vertical cross-sections of relative humidity with unstable stratification (demarcated by the white enclosed area) along the transect indicated by the red line in Fig. 1. Black solid lines represent isotherms, while black dashed lines denote the location of the observation site. **(d–i)** Meteorological fields at the 650 and 800 hPa levels, with geopotential height contours, during the experimental period over the Dunhuang region. White regions indicate elevated mountain terrain.

layer episode, potential temperature was relatively low, with cold air masses dominating. The wind direction was predominantly northerly, and geopotential height increased from northeast to southwest. Although a cyclone was located to the southwest of the region, no prominent large-scale synoptic system or strong convective activity directly affected the Minqin site. This indicates that atmospheric stratification at this level was relatively stable, favouring aerosol confinement below this layer. During elevated aerosol layer episode, the site was situated near the boundary between cold and warm air masses (Fig. 10e). This frontal transition zone led to enhanced relative humidity at this level (Zhang et al., 2007). During this process, warm, moist air ascended over the colder air mass, likely forming a frontal inversion that suppressed vertical motion and inhibited atmospheric mixing (Feng et al., 2023). Following the elevated aerosol layer episode, warm and moist air masses became more influential over the site, and the high-relative-humidity layer persisted near the upper boundary of the unstable layer. Additionally, the mountain–valley circulation near the Qilian Mountains was more evident in the Minqin case (Fig. 10g–i). This terrain-induced circulation, together with the daytime thermal forcing, may have facilitated the horizontal transport of elevated aerosols toward the Qilian Mountains under favourable background winds. Therefore, Fig. 10 indicates that the Minqin case shared the common daytime uplift–

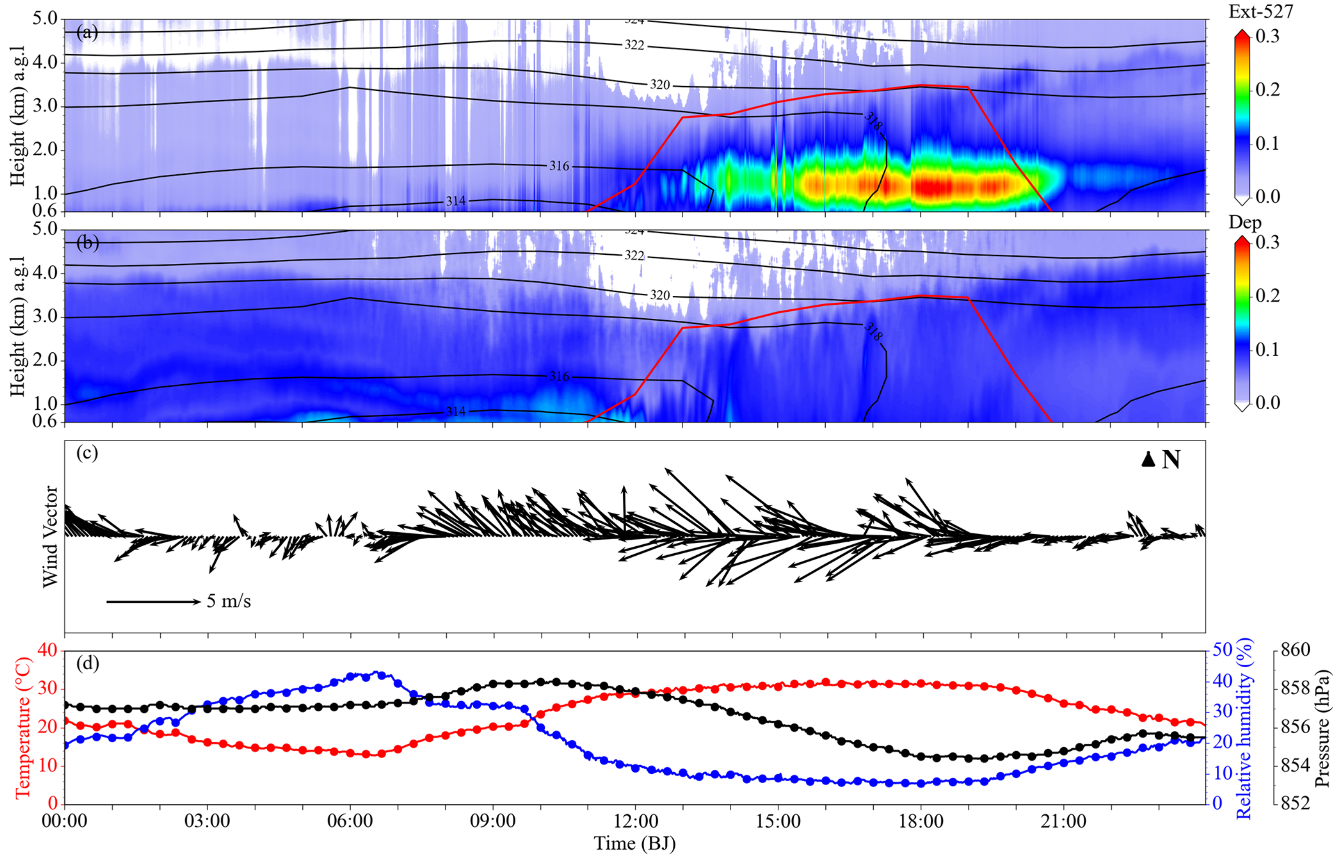


**Figure 9.** Time series of aerosol vertical distribution and meteorological parameters at Minqin on 14 June 2010. **(a)** Time–height cross-sections of aerosol extinction coefficient and **(b)** depolarization ratio derived from MPL lidar, with potential temperature contours (black lines) and boundary layer height (red lines) from ERA5. **(c)** Wind vectors measured by an automatic meteorological station (model WXT520), and **(d)** temperature, relative humidity, and pressure.

accumulation mechanism observed at Dunhuang, but with a stronger influence from the humid stable layer and terrain-induced circulation.

As shown in Fig. 11, during cases when elevated aerosol layers occurred at Dunhuang and Minqin, the potential temperature below 3 km at both sites exhibited a positive anomaly of 3–5 K (Fig. 11a–c and m–o), indicating a warmer-than-average thermal state compared with the average boundary layer potential temperature (∼ 310 K) at the two sites during the experiment period. Meanwhile, relative humidity below this altitude was generally 5 %–10 % lower than the average value (∼ 30 %) (Fig. 11d–f and p–r), indicating distinctly dry and warm anomalous meteorological conditions in the lower atmosphere. Notably, during cases at Minqin, positive relative humidity anomalies of 5 %–15 % appeared above approximately 3 km, consistent with those shown in Fig. 10a–c. This suggests that the region may be influenced by the interaction of cold and warm air masses under some synoptic conditions. This vertical humidity distribution is consistent with previous findings that high-humidity conditions near the top of the boundary layer favour the retention and accumulation of aerosols within the boundary layer (Altstädter et al., 2018). In contrast, when elevated aerosol layers did not occur, the potential temperature at both sites showed a negative anomaly of 1–6 K (Fig. 11g–i and s–u), and relative humidity was 5 %–25 % higher than the average state (Fig. 11j–l and v–x). To further support the composite anomaly analysis, daily samples were statistically compared under conditions with and without elevated aerosol layers within the main height range and occurrence period of elevated aerosol layers (Fig. S3 in the Supplement). The results show that daily potential temperature anomalies were generally higher, whereas daily relative humidity anomalies were generally lower, under conditions with elevated aerosol layers at both Dunhuang and Minqin sites. This is consistent with the dry and warm anomalies revealed by the composite analysis. The non-parametric test results indicate statistically distinguishable differences between the two groups, with significance levels varying between variables and sites. These daily statistics provide additional support that the dry and warm thermodynamic conditions associated with elevated aerosol layers are also evident in day-to-day variabil-

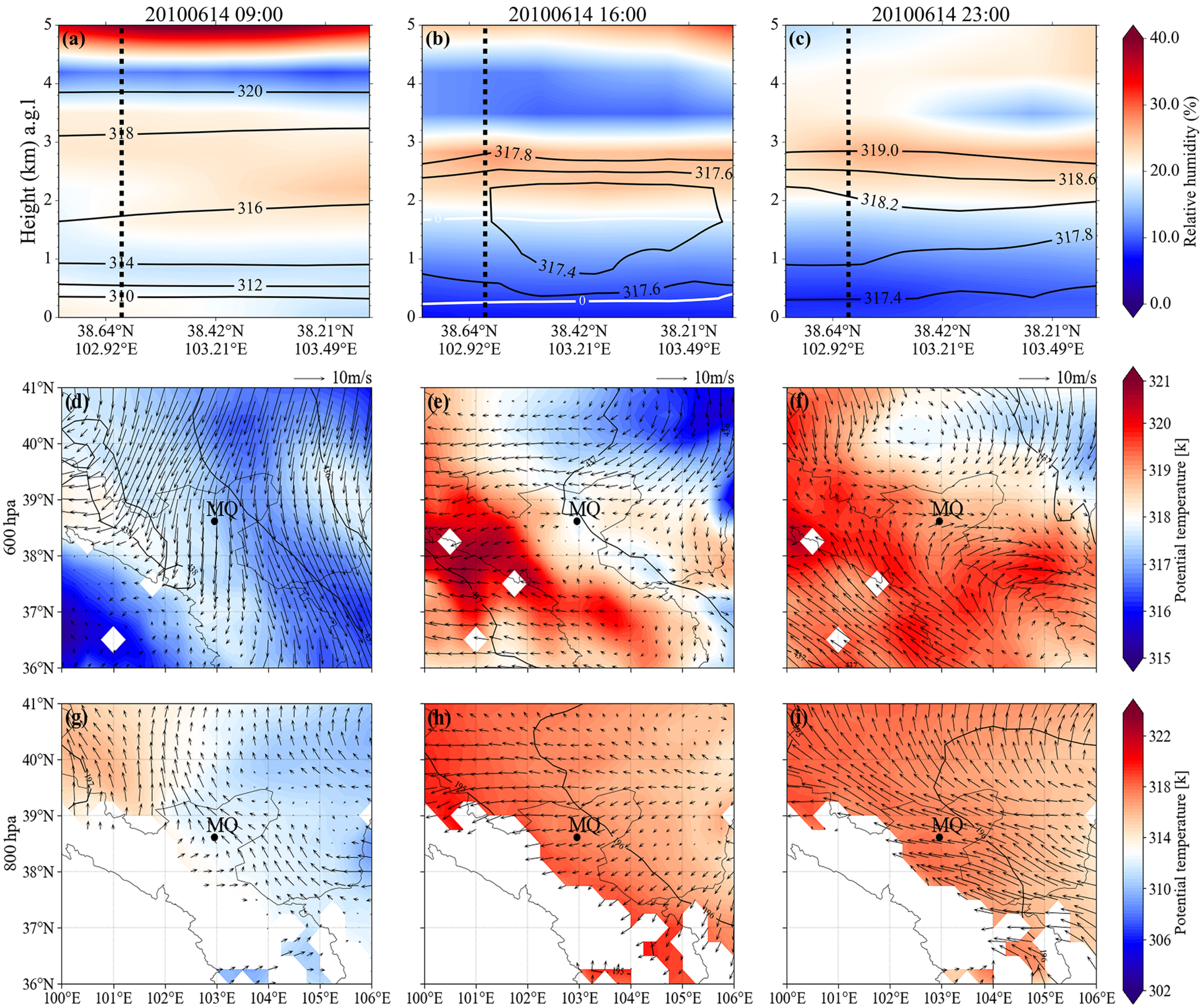


**Figure 10.** Thermal and dynamical fields at Minqin on 14 June 2010. **(a–c)** Vertical cross-sections of relative humidity with unstable stratification (demarcated by the white enclosed area) along the transect indicated by the red line in Fig. 1. Black solid lines represent isotherms, while black dashed lines denote the location of the observation site. **(d–i)** Meteorological fields at the 600 and 800 hPa levels, with geopotential height contours, during the experimental period over the Minqin region. White regions indicate elevated mountain terrain.

ity. Based on these observations, the occurrence of elevated aerosol layers was closely associated with boundary layer temperature and humidity anomalies. Most elevated aerosol layer events occurred under the anomalously dry and warm conditions, characterised by positive potential temperature anomalies and negative relative humidity anomalies. These lower-atmospheric conditions were conducive to enhanced sensible heating, reduced static stability, and stronger vertical mixing within the daytime boundary layer. Consequently, daytime thermal mixing and local thermally driven circulations can promote the upward transport of aerosols from the lower atmosphere. Meanwhile, the relatively low-humidity air is characterized by a higher lifting condensation level (Lal et al., 2024), which indicates that aerosol uplift under these conditions is more closely related to dry thermal mixing than to moist convective development. When the lifted aerosols reach the stable stratification near the boundary layer top, further vertical dispersion is suppressed, thereby favouring aerosol accumulation and persistence aloft.

Overall, the representative cases and composite anomalies indicate that elevated aerosol layer formation at both sites was associated with a common daytime uplift–accumulation mechanism. Positive potential temperature anomalies and negative relative humidity anomalies within the daytime boundary layer favoured sensible heating, reduced static stability, and enhanced vertical mixing, while stable stratifica-

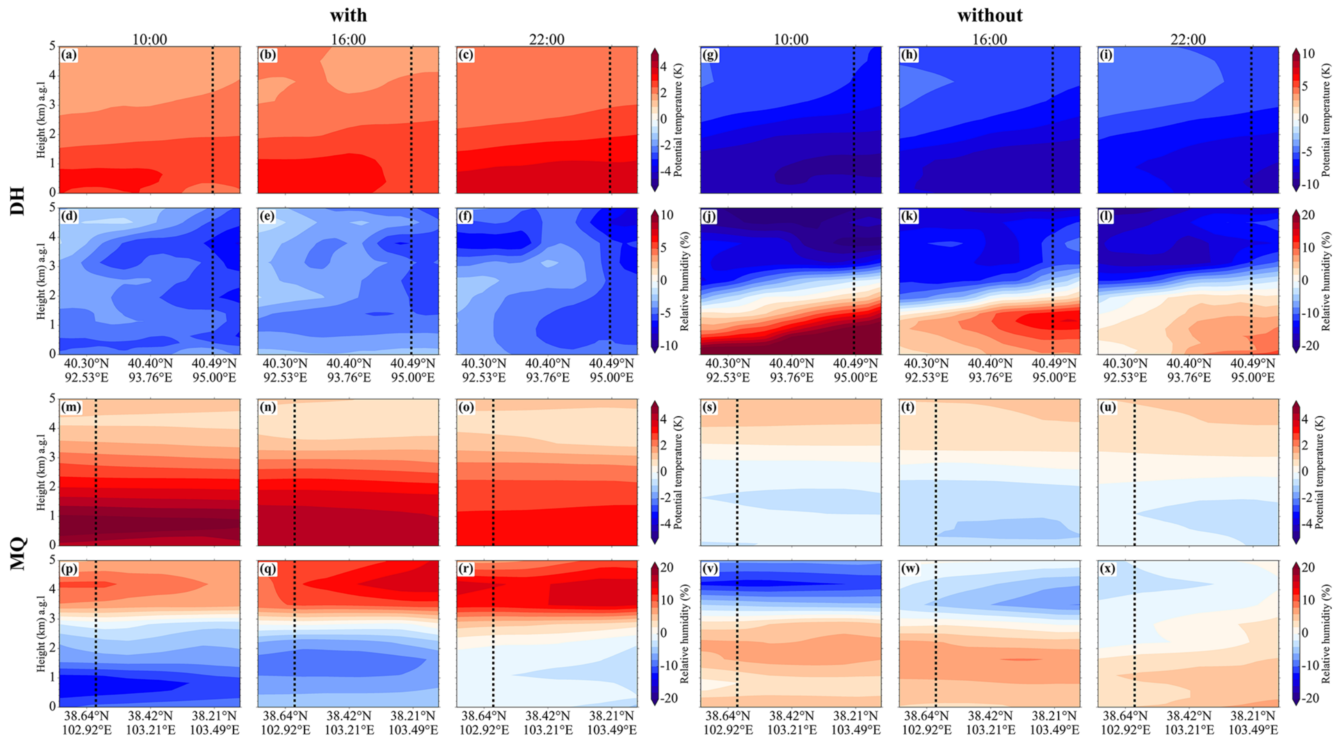


**Figure 11.** Anomalies of potential temperature and relative humidity between the mean states during periods with and without elevated aerosol layers and the summer climatological state at Dunhuang and Minqin.

tion near the boundary layer top limited further upward dispersion and promoted aerosol accumulation aloft. Terrain-induced local circulations further modulated the horizontal transport of the elevated aerosol layers. These results suggest that the similar thermodynamic evolution observed in the Dunhuang and Minqin cases reflects a common physical process rather than two independent case-specific phenomena. Based on these findings, a simplified conceptual prediction model for elevated aerosol layers can be constructed, with key early-warning indicators being positive anomalies in boundary layer potential temperature and negative anomalies in boundary layer relative humidity. When both indicators are satisfied simultaneously, this can be identified as a meteorological condition favourable for the occurrence of elevated aerosol layers, although additional long-term observations and model simulations are still needed to further evaluate its predictive applicability.

During both experimental periods, $PM_{10}$ mass concentration observations were available only at Dunhuang. Here, the conversion method described in Sect. 2 was used to assess the air pollution levels of elevated aerosol layers. As shown in Fig. 12, $PM_{10}$ concentration at the near-surface and at the peak of elevated aerosol layers are presented. The average near-surface $PM_{10}$ concentration across all observations was $129.6 \pm 212.0\,\mu g\,m^{-3}$ during the entire experimental period. During elevated aerosol layer episodes, the near-surface average $PM_{10}$ concentration decreased to $40.8 \pm 30.4\,\mu g\,m^{-3}$, whereas the average $PM_{10}$-equivalent mass concentration estimated from the aerosol extinction coefficient at the peak of the elevated aerosol layers reached $203.3 \pm 106.6\,\mu g\,m^{-3}$. The peak $PM_{10}$-equivalent concentration is nearly five times higher than that at the near-surface. This estimated concentration approaches levels observed during severe haze events. For instance, previous studies reported that a severe haze event in Beijing, China recorded an average $PM_{10}$ concentration of $265.2 \pm 157.1\,\mu g\,m^{-3}$ (Wang et al., 2015). $PM_{10}$ concentrations during haze and dust events in South Korea reached $163.9 \pm 25.0\,\mu g\,m^{-3}$ and $211.3 \pm 57.5\,\mu g\,m^{-3}$, respectively (Jung et al., 2017; Seo et al., 2017). This clearly indicates that even when surface pollution is low or negligible, a highly concentrated pollutant aerosol layer may exist in the upper boundary layer. Although $PM_{10}$ concentration observations are only available from Dunhuang, the periods of elevated aerosol layer occurrence during daytime and their associated thermodynamic conditions are similar at both sites, as shown in Figs. 7, 9 and 11. Therefore, it can be inferred that such elevated aerosol layers may occur throughout the Hexi Corridor region under similar meteorological conditions, exerting a significant impact on the regional environment. These findings highlight that, when assessing air quality and developing pollution control strategies, reliance solely on surface-level monitoring is insufficient. Instead, elevated aerosol layers within the boundary layer should be comprehensively considered, as their formation and disper-

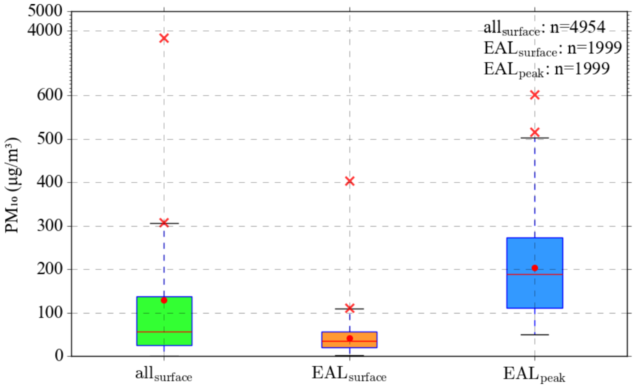


**Figure 12.** Boxplots of $PM_{10}$ concentrations during the experiment at the Dunhuang site, including surface values for all days, surface values during elevated aerosol layer (EAL) days, and peak values within elevated aerosol layers. The red lines represent the median, red dots indicate the mean values, the box edges denote the 25th and 75th percentiles (Q1 and Q3), and the whiskers represent non-outlier data points. Outliers (values beyond $Q3 + 1.5 \times IQR$ or below $Q1 - 1.5 \times IQR$) are marked with red crosses, with only the minimum and maximum outliers labelled for clarity. Under a normal distribution, the whiskers encompass approximately 99 % of the data.

sion are closely related to surface pollutant level (Dong et al., 2022).

The presence of elevated aerosol layers not only increases air pollution levels over the Hexi Corridor region but also exerts significant regional radiative effects. Simulated shortwave radiative forcing results for two elevated aerosol layer events – observed on 21 April 2012 at Dunhuang and on 14 June 2010 at Minqin – are presented (Fig. 13a). At the surface (SFC), the average shortwave radiative forcing at Dunhuang was $-22.66\,W\,m^{-2}$, with a significantly larger magnitude than that at Minqin ($-13.60\,W\,m^{-2}$). This indicates a stronger surface cooling effect induced by elevated aerosol layers at Dunhuang. In addition, these effects reduce solar radiation reaching the surface during daytime and can directly affect the efficiency of photovoltaic power generation. This value exceeds the shortwave radiative forcing at the SFC reported for a moderate dust event ($-19.5\,W\,m^{-2}$) (Li et al., 2025) and is comparable to the $-23\,W\,m^{-2}$ observed during dust events (Marsli et al., 2025). The value at Minqin is stronger than that for a light dust event ($-12.0\,W\,m^{-2}$) reported by Li et al. (2025), and is comparable to mineral dust events ($-13.65\,W\,m^{-2}$) reported by Barragan et al. (2020). Radiative forcing at the top of atmosphere (TOA) was negative at both sites, averaging $-8.92\,W\,m^{-2}$ at Dunhuang, with a larger magnitude than $-4.49\,W\,m^{-2}$ at Minqin, which is close to the $-4\,W\,m^{-2}$ reported for dust events (Marsli et al., 2025). This value is comparable to a mineral dust event ($-9.1\,W\,m^{-2}$) observed over the Iberian Peninsula (Barragan et al., 2020) but significantly higher than $-2.7$ and $-4.0\,W\,m^{-2}$ during two other dust events at Dunhuang recorded by Bi et al. (2014). These findings demonstrate that elevated aerosol layers exert a cooling effect in both regions. Elevated aerosol layers at Dunhuang exert a more pronounced effect on increasing the planetary albedo, thereby producing a stronger suppression of the surface radiation budget. Additionally, the average atmospheric (ATM) shortwave radiative forcing at Dunhuang is $13.74\,W\,m^{-2}$, higher than $9.10\,W\,m^{-2}$ at Minqin. This suggests that elevated aerosol layers at Dunhuang are more efficient at intercepting and redistributing solar radiation, with atmospheric radiative forcing higher than $5.1\,W\,m^{-2}$ reported for a dust event (Bran et al., 2018), but lower than $16.94\,W\,m^{-2}$ reported for a mineral dust event over the Iberian Peninsula (Barragan et al., 2020). Atmospheric (ATM) shortwave radiative forcing reflects the energy absorbed by aerosols and converted into heat within the atmosphere. The peak shortwave heating rate (Jangid et al., 2024) reached $0.74\,K\,d^{-1}$ at Dunhuang and $0.44\,K\,d^{-1}$ at Minqin, with the value at Dunhuang comparable to the peak heating rate ($\sim 0.7\,K\,d^{-1}$) reported for a light dust event (Li et al., 2025). The mean shortwave heating rates (SHR) at both sites ($0.23\,K\,d^{-1}$ at Dunhuang and $0.14\,K\,d^{-1}$ at Minqin) were higher than those observed during several dust events at Dunhuang (Bi et al., 2014) (e.g., 0.1 and $0.14\,K\,d^{-1}$ on 9 and 10 April 2012, respectively), as well as those recorded over Issyk-Kul Lake ($0.08\,K\,d^{-1}$) (Gan et al., 2026) and southern Portugal ($0.11\,K\,d^{-1}$) (Valenzuela et al., 2016). This indicates that elevated aerosol layers absorb solar shortwave radiation, leading to significant atmospheric heating. This may influence regional weather processes and climate feedback mechanisms by altering the local thermal structure and vertical stability (Huang et al., 2009).

Considering snow cover conditions in the Qilian Mountains, seasonal snow is primarily distributed at altitudes of 3–4 km (equivalent to 1.5–2.5 km a.g.l.) (Guo et al., 2021), which coincides with the altitude range of elevated aerosol layers. After deposition in the Qilian Mountains, these pollutants significantly reduce snow albedo, enabling the surface to absorb more solar radiation. Simultaneously, as indicated by the SHR of the elevated aerosol layer, the layer itself maintains a relatively high temperature due to its absorption of shortwave radiation, and the resulting heat further accelerates snowmelt. This combined effect may accelerates snowmelt and glacier retreat. Therefore, radiative forcing associated with elevated aerosol layer may induce regional warming in the Qilian Mountains, similar to the warming effect of brown clouds over the Indian Peninsula, which accelerates snowmelt in the Himalayas (Ramanathan et al., 2007). This is of considerable concern, as it is directly linked to regional water security and storage. In addition, the Hexi Corridor is also an important solar energy base, the elevated aerosol layer weakens the solar radiation reaching the surface during daytime, thereby directly affecting photovoltaic power generation efficiency (Wang et al., 2026).

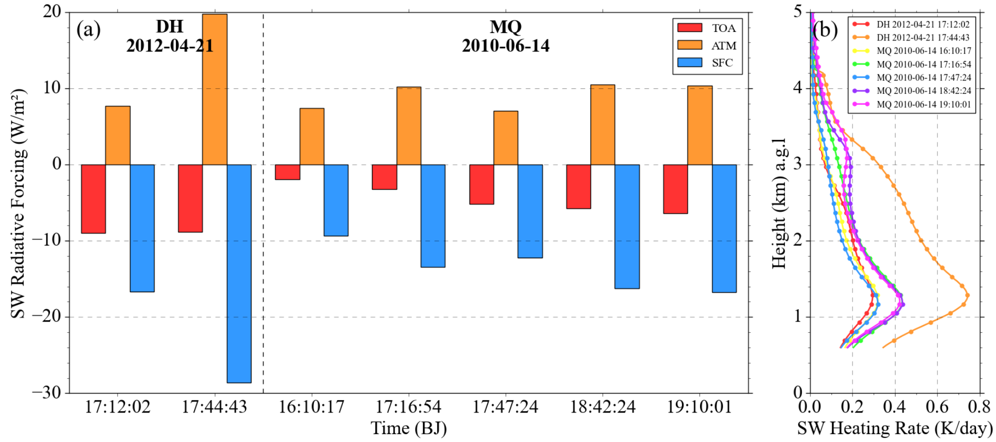


**Figure 13.** Radiative effects of elevated aerosol layers. **(a)** Histograms of aerosol shortwave radiative forcing (SWRF) at Dunhuang and Minqin, with red, orange, and blue bars representing the surface (SFC), atmosphere (ATM), and top of the atmosphere (TOA), respectively; **(b)** vertical profiles of shortwave heating rate at Dunhuang and Minqin.

## 4 Conclusion

Based on intensive observation campaigns in 2010 and 2012 over the Hexi Corridor in Northwest China, this study first reveals the occurrence of elevated aerosol layers within the daytime mixed layer in this region and further examines their vertical distribution characteristics, formation mechanisms from a diurnal perspective, and environmental and radiative effects. The results show that distinct elevated aerosol layers occur at approximately 0.6–2 km during daytime at both Dunhuang and Minqin. Excluding dust events, the occurrence frequencies of elevated aerosol layers are approximately 82 % and 44 % at Dunhuang and Minqin, respectively, with peak occurrence concentrated in May and June. EALs at Dunhuang were more frequently dust-influenced, whereas those at Minqin were more strongly influenced by fine-mode and/or anthropogenic aerosols; both aerosol types nevertheless occurred at both sites. The formation of elevated aerosol layers is controlled by a coupled thermodynamic process: daytime surface heating reduces static stability and enhances vertical mixing, facilitating the upward transport and accumulation of aerosols at the base of the stable layer. Under favorable wind regimes, daytime mountain–valley circulations may further transport these elevated aerosol layers toward the adjacent Qilian Mountains. Additionally, conditions at Minqin are influenced by frontal inversions and water vapour. Thus, a simplified conceptual model for the prediction of elevated aerosol layer occurrence is proposed, based on positive anomalies in potential temperature and negative anomalies in relative humidity within the boundary layer. Regarding environmental impacts, the peak Extinction-derived $PM_{10}$-equivalent mass concentration within the elevated aerosol layer ($203.3 \pm 106.6\,\mu g\,m^{-3}$) is approximately five times higher than that at the surface ($40.8 \pm 30.4\,\mu g\,m^{-3}$), indicating that reliance solely on surface observations would substantially underestimate the regional pollution burden. Meanwhile, such layers enhance the atmospheric shortwave heating rate by up to $0.7\,K\,d^{-1}$, a magnitude comparable to that associated with light dust loading. Notably, the mean shortwave heating rates at both sites are higher than those reported during several dust events at Dunhuang. Furthermore, elevated aerosol layers are likely to accelerate glacier retreat and snow melt by reducing snow/ice albedo and enhancing radiative absorption, thereby posing a potential threat to regional water resource security, particularly under the influence of mountain–valley winds.

This study provides valuable observational evidence for the existence of elevated aerosol layers in the Hexi Corridor region, and underscores their relevance to regional air pollution prevention and control, ecosystem protection in complex terrains, and water resource security in ecologically sensitive areas of northwest China. It should be noted that the intensive observations used in this study were conducted in 2010 at Minqin and in 2012 at Dunhuang. Therefore, the occurrence frequencies, dominant aerosol types, $PM_{10}$-equivalent mass concentrations, and radiative effects reported here should be interpreted as representative of the specific campaign periods rather than as a present-day climatology of the Hexi Corridor. Over the past decade, changes in anthropogenic emissions, dust activity, aerosol composition, land-surface conditions, and regional atmospheric environments may have affected the occurrence and characteristics of elevated aerosol layers. Nevertheless, the thermodynamic mechanism identified in this study, including daytime surface heating, dry lower-atmospheric conditions, upward transport of near-surface aerosols, and accumulation below stable stratification, is physically based and may remain applicable under similar meteorological and source conditions. However, the limited observations remain insufficient for a comprehensive understanding of the formation, maintenance, long-term evolution, and regional impacts of elevated aerosol layers. Additional long-term field observations and model simulations across other parts of the Hexi Corridor and the adjacent Qilian Mountains are needed to further investigate the present-day occurrence, long-term evolution, composition changes, and regional impacts of elevated aerosol layers.

**Code and data availability.** The ERA-5 reanalysis data are available from the ECMWF at https://doi.org/10.24381/cds.adbb2d47 (Hersbach et al., 2023). The AERONET data are provided by the NASA and can be accessed at https://aeronet.gsfc.nasa.gov/ (last access: 13 June 2025). The HYSPLIT data is sourced from the NOAA and can be accessed at https://www.arl.noaa.gov/hysplit/ (last access: 23 October 2025). The SBDART model used in this study is publicly available at https://github.com/paulricchiazzi/SBDART (last access: 20 June 2025).

**Supplement.** The supplement related to this article is available online at https://doi.org/10.5194/acp-26-11111-2026-supplement.

**Author contributions.** ZL: Writing – original draft, Software, Resources, Methodology, Investigation, Formal analysis, Data curation. TZ: Writing – review and editing, Writing – original draft, Supervision, Project administration, Funding acquisition, Data curation, Conceptualization. ZPL: Software, Resources, Methodology, Investigation, Formal analysis, Data curation. YG: Software, Resources, Methodology, Investigation, Formal analysis. DW: Software, Resources, Methodology, Investigation, Formal analysis. PZ: Methodology, Resources, Software, Data curation. KZ: Software, Resources, Methodology, Data curation. QG: Software, Resources, Methodology, Data curation. XL: Software, Resources, Methodology, Data curation. ZH: Writing – review and editing, Validation, Supervision, Project administration, Data curation, Conceptualization. JB: Writing – review and editing, Writing – original draft, Supervision, Project administration, Data curation, Conceptualization. LY: Writing – review and editing, Writing – original draft, Supervision, Project administration, Data curation, Conceptualization. LW: Writing – review and editing, Writing – original draft, Supervision, Project administration, Data curation, Conceptualization.

**Competing interests.** The contact author has declared that none of the authors has any competing interests.

**Disclaimer.** Publisher's note: Copernicus Publications remains neutral with regard to jurisdictional claims made in the text, published maps, institutional affiliations, or any other geographical representation in this paper. The authors bear the ultimate responsibility for providing appropriate place names. Views expressed in the text are those of the authors and do not necessarily reflect the views of the publisher.

**Acknowledgements.** The authors would like to express their sincere thanks to all personnel involved in the intensive field observations. We are grateful to the ERA5 team for providing the reanalysis data used in this study. We appreciate the Earth Space Research Group, Institute for Computational Earth System Science, University of California, Santa Barbara, for their contribution to the SBDART model used in this study. We also thank the anonymous reviewers for their insightful and valuable comments.

**Financial support.** This research was funded by Fundamental and Interdisciplinary Disciplines Breakthrough Plan of the Ministry of Education of China (grant no. JYB2025XDXM910), the National Science Foundation of China (grant nos. 42427803 and 42475078), Gansu Longyuan Youth Talents (2025), the Gansu Provincial Science and Technology Program (grant no. 23JRRA1032), and the China "111" Project (grant no. B25040).

**Review statement.** This paper was edited by Suvarna Fadnavis and reviewed by two anonymous referees.

## References

Albergel, C., Dutra, E., Munier, S., Calvet, J.-C., Munoz-Sabater, J., de Rosnay, P., and Balsamo, G.: ERA-5 and ERA-Interim driven ISBA land surface model simulations: which one performs better?, Hydrol. Earth Syst. Sci., 22, 3515–3532, https://doi.org/10.5194/hess-22-3515-2018, 2018.

Altstädter, B., Platis, A., Jähn, M., Baars, H., Lückerath, J., Held, A., Lampert, A., Bange, J., Hermann, M., and Wehner, B.: Airborne observations of newly formed boundary layer aerosol particles under cloudy conditions, Atmos. Chem. Phys., 18, 8249–8264, https://doi.org/10.5194/acp-18-8249-2018, 2018.

Barragan, R., Molero, F., Granados-Muñoz, M., Salvador, P., Artíñano, B., and Pujadas, M.: Feasibility of Ceilometers Data to Estimate Radiative Forcing Values: Application to Different Conditions around the COVID-19 Lockdown Period, Remote Sens.-Basel, 12, 3699, https://doi.org/10.3390/rs12223699, 2020.

Bellini, A., Diémoz, H., Gobbi, G. P., Di Liberto, L., Bracci, A., and Barnaba, F.: Aerosols in the Mixed Layer and Mid-Troposphere from Long-Term Data of the Italian Automated Lidar-Ceilometer Network (ALICENET) and Comparison with the ERA5 and CAMS Models, Remote Sens.-Basel, 17, 372, https://doi.org/10.3390/rs17030372, 2025.

Bi, J., Shi, J., Xie, Y., Liu, Y., Takamura, T., and Khatri, P.: Dust Aerosol Characteristics and Shortwave Radiative Impact at a Gobi Desert of Northwest China during the Spring of 2012, J. Meteorol. Soc. Jpn., 92A, 33–56, https://doi.org/10.2151/jmsj.2014-A03, 2014.

Bi, J., Huang, J., Shi, J., Hu, Z., Zhou, T., Zhang, G., Huang, Z., Wang, X., and Jin, H.: Measurement of scattering and absorption properties of dust aerosol in a Gobi farmland region of northwestern China – a potential anthropogenic influence, Atmos. Chem. Phys., 17, 7775–7792, https://doi.org/10.5194/acp-17-7775-2017, 2017.

Boselli, A., Armenante, M., D'Avino, L., D'Isidoro, M., Pisani, G., Spinelli, N., and Wang, X.: Atmospheric Aerosol Characterization Over Naples During 2000–2003 EARLINET Project: Planetary Boundary-Layer Evolution and Layering, Bound.-Lay. Meteorol., 132, 151–165, https://doi.org/10.1007/s10546-009-9382-6, 2009.

Bran, S., Jose, S., and Srivastava, R.: Investigation of optical and radiative properties of aerosols during an intense dust storm: A regional climate modeling approach, J. Atmos. Sol.-Terr. Phy., 168, 21–31, https://doi.org/10.1016/j.jastp.2018.01.003, 2018.

Cacciani, M., Kossmann, M., Knievel, J. C., Giovannini, L., Gutmann, E. D., and Zardi, D.: Meteorological Applications Benefiting from an Improved Understanding of Atmospheric Exchange Processes over Mountains, Atmosphere-Basel, 9, 371, https://doi.org/10.3390/atmos9100371, 2018.

Che, H., Xia, X., Zhao, H., Li, L., Gui, K., Zheng, Y., Song, J., Qi, B., Zhu, J., Miao, Y., Wang, Y., Wang, Z., Wang, H., Dubovik, O., Holben, B., Chen, H., Shi, G., and Zhang, X.: Aerosol optical and radiative properties and their environmental effects in China: A review, Earth-Sci. Rev., 248, 104634, https://doi.org/10.1016/j.earscirev.2023.104634, 2024.

Chen, Q., Yin, Y., Jin, L.-j., Xiao, H., and Zhu, S.-c.: The effect of aerosol layers on convective cloud microphysics and precipitation, Atmos. Res., 101, 327–340, https://doi.org/10.1016/j.atmosres.2011.03.007, 2011.

Cheng, Y., Dai, T., Li, J., and Shi, G.: Measurement Report: Determination of aerosol vertical features on different timescales over East Asia based on CATS aerosol products, Atmos. Chem. Phys., 20, 15307–15322, https://doi.org/10.5194/acp-20-15307-2020, 2020a.

Dang, J., Xie, X., and Wen, X.: Evaluation of Boundary Layer Characteristics at Mount Si'e Based on UAV and Lidar Data, Remote Sens.-Basel, 16, 3816, https://doi.org/10.3390/rs16203816, 2024.

De Wekker, S. F. J., Kossmann, M., Knievel, J. C., Giovannini, L., Gutmann, E. D., and Zardi, D.: Meteorological Applications Benefiting from an Improved Understanding of Atmospheric Exchange Processes over Mountains, Atmosphere-Basel, 9, 371, https://doi.org/10.3390/atmos9100371, 2018.

DeRepentigny, P.: When fire and ice meet, Nat. Clim. Change, 14, 1224–1225, https://doi.org/10.1038/s41558-024-02183-z, 2024.

Diya, M., Kuppili, S. K., and Nagendra, S. M. S.: Air quality in different urban hotspots in a metropolitan city in India and the environmental implication, Environ. Monit. Assess., 196, https://doi.org/10.1007/s10661-024-13272-z, 2024.

Dong, Q., Huang, Z., Li, W., Li, Z., Song, X., Liu, W., Wang, T., Jianrong, B., and Shi, J.: Polarization Lidar Measurements of Dust Optical Properties at the Junction of the Taklimakan Desert–Tibetan Plateau, Remote Sens.-Basel, 14, 558, https://doi.org/10.3390/rs14030558, 2022.

Du, Q., Zhao, C., Zhang, M., Dong, X., Chen, Y., Liu, Z., Hu, Z., Zhang, Q., Li, Y., Yuan, R., and Miao, S.: Modeling diurnal variation of surface $PM_{2.5}$ concentrations over East China with WRF-Chem: impacts from boundary-layer mixing and anthropogenic emission, Atmos. Chem. Phys., 20, 2839–2863, https://doi.org/10.5194/acp-20-2839-2020, 2020.

Dubovik, O., Holben, B., Eck, T. F., Smirnov, A., Kaufman, Y. J., King, M. D., Tanré, D., and Slutsker, I.: Variability of Absorption and Optical Properties of Key Aerosol Types Observed in Worldwide Locations, J. Atmos. Sci., 59, 590–608, https://doi.org/10.1175/1520-0469(2002)059<0590:VOAAOP>2.0.CO;2, 2002.

Feng, X., Zhang, Z., Guo, J., and Wang, S.: Multilayer inversion formation and evolution during persistent heavy air pollution events in the Sichuan Basin, China, Atmos. Res., 286, 106691, https://doi.org/10.1016/j.atmosres.2023.106691, 2023.

Fountoulakis, I., Papachristopoulou, K., Proestakis, E., Amiridis, V., Kontoes, C., and Kazadzis, S.: Effect of Aerosol Vertical Distribution on the Modeling of Solar Radiation, Remote Sens.-Basel, 14, 1143, https://doi.org/10.3390/rs14051143, 2022.

Gan, Y., Zhang, Z., Chu, W., Ding, J., and Ren, Y.: Assessment and prediction of dust emissions, deposition and radiation forcing in Central Asia, Atmos. Chem. Phys., 26, 3881–3900, https://doi.org/10.5194/acp-26-3881-2026, 2026.

Guo, J., Yin, Y., Xu, M., Wu, J., Liu, D., Fan, W., and Lu, P.: Numerical study of aerosol radiative forcing over East Asia and the impacts of cloud coverage and relative humidity, Atmos. Res., 273, 106168, https://doi.org/10.1016/j.atmosres.2022.106168, 2022.

Guo, Z., Wang, N., Shen, B., Gu, Z., Wu, Y., and Chen, A.: Recent Spatiotemporal Trends in Glacier Snowline Altitude at the End of the Melt Season in the Qilian Mountains, China, Remote Sens.-Basel, 13, 4935, https://doi.org/10.3390/rs13234935, 2021.

Haeffelin, M., Ribaud, J.-F., Céspedes, J., Dupont, J.-C., Lemonsu, A., Masson, V., Nagel, T., and Kotthaus, S.: Impact of boundary layer stability on urban park cooling effect intensity, Atmos. Chem. Phys., 24, 14101–14122, https://doi.org/10.5194/acp-24-14101-2024, 2024.

Hara, K., Takashima, H., Yoshino, A., Takami, A., Nishita-Hara, C., Fujiyoshi, Y., and Hayashi, M.: Seasonal variations of diurnal cycles of aerosols and gases in the Fukuoka Plain, Japan: Effects of local meteorology and atmospheric chemistry, Atmos. Environ., 289, https://doi.org/10.1016/j.atmosenv.2022.119318, 2022.

Hersbach, H., Bell, B., Berrisford, P., Biavati, G., Horányi, A., Muñoz Sabater, J., Nicolas, J., Peubey, C., Radu, R., Rozum, I., Schepers, D., Simmons, A., Soci, C., Dee, D., and Thépaut, J.-N.: ERA5 hourly data on single levels from 1940 to present, Copernicus Climate Change Service (C3S) Climate Data Store (CDS) [data set], https://doi.org/10.24381/cds.adbb2d47, 2023.

Holben, B. N., Eck, T. F., Slutsker, I., Tanré, D., Buis, J. P., Setzer, A., Vermote, E., Reagan, J. A., Kaufman, Y. J., Nakajima, T., Lavenu, F., Jankowiak, I., and Smirnov, A.: AERONET – A Federated Instrument Network and Data Archive for Aerosol Characterization, Remote Sens. Environ., 66, 1–16, https://doi.org/10.1016/S0034-4257(98)00031-5, 1998.

Hou, X., Fei, D., Kang, H., Zhang, Y., and Gao, J.: Seasonal statistical analysis of the impact of meteorological factors on fine particle pollution in China in 2013–2017, Nat. Hazards, 93, 677–698, https://doi.org/10.1007/s11069-018-3315-y, 2018.

Houze Jr., R. A.: Mesoscale convective systems, Reviews of Geophysics, 42, https://doi.org/10.1029/2004RG000150, 2004.

Hu, Y., Yu, H., Kang, S., Yang, J., Rai, M., Yin, X., Chen, X., and Chen, P.: Aerosol–meteorology feedback diminishes the transboundary transport of black carbon into the Tibetan Plateau, Atmos. Chem. Phys., 24, 85–107, https://doi.org/10.5194/acp-24-85-2024, 2024.

Huang, J., Fu, Q., Su, J., Tang, Q., Minnis, P., Hu, Y., Yi, Y., and Zhao, Q.: Taklimakan dust aerosol radiative heating derived from CALIPSO observations using the Fu-Liou radiation model with CERES constraints, Atmos. Chem. Phys., 9, 4011–4021, https://doi.org/10.5194/acp-9-4011-2009, 2009.

Huang, J., Wang, T., Wencai, W., Li, Z., and Yan, H.: Climate effects of dust aerosols over East Asian arid and semiarid regions, J. Geophys. Res.-Atmos., 119, https://doi.org/10.1002/2014JD021796, 2014.

Huang, Z., Huang, J., Jianrong, B., Wang, T., Zhou, T., Dong, Q., Shi, J., Qiantao, L., Li, W., Li, Z., Song, X., Liu, W., Wang, H., and Niu, Z.: Dust observation by a ground-based lidar network along the global dust belt, E3S Web Conf., 575, 02006, https://doi.org/10.1051/e3sconf/202457502006, 2024.

Huang, Z., Dong, Q., Zhou, T., Jianrong, B., Chen, R., Qiantao, L., Abdullaev, S., Nozirov, D., Alam, K., Wang, T., Li, W., Li, Z., Song, X., and Liu, W.: Vertical distribution, optical properties, and source attribution of summer dust in southern Tajikistan: ground-based observations and model results, Atmos. Environ., 361, 121514, https://doi.org/10.1016/j.atmosenv.2025.121514, 2025.

Huige, D., Siwen, L., Yun, Y., Dengxin, H., and Jianyu, W.: Observational study of the vertical aerosol and meteorological factor distributions with respect to particulate pollution in Xi'an, Atmos. Environ., 247, 118215, https://doi.org/10.1016/j.atmosenv.2021.118215, 2021.

Huszar, P., Karlický, J., Ďoubalová, J., Šindelářová, K., Nováková, T., Belda, M., Halenka, T., Žák, M., and Pišoft, P.: Urban canopy meteorological forcing and its impact on ozone and $PM_{2.5}$: role of vertical turbulent transport, Atmos. Chem. Phys., 20, 1977–2016, https://doi.org/10.5194/acp-20-1977-2020, 2020.

Jangid, M., Sankhla, T. S., Singh, S., and Mishra, A. K.: Radiative effect of atmospheric Brown clouds over the Indo-Gangetic plain, Atmos. Pollut. Res., 15, 102085, https://doi.org/10.1016/j.apr.2024.102085, 2024.

Jia, S., Sarkar, S., Zhang, Q., Wang, X., Wu, L., Chen, W., Huang, M., Zhou, S., Zhang, J., Yuan, L., and Yang, L.: Characterization of diurnal variations of $PM_{2.5}$ acidity using an open thermodynamic system: A case study of Guangzhou, China, Chemosphere, 202, 677–685, https://doi.org/10.1016/j.chemosphere.2018.03.127, 2018.

Jian, B., Ma, Z., Liu, Q., Li, Z., Deng, L., Nie, H., Liu, C., Zhao, C., Sun, J., and Shen, X.: An advanced double-moment cloud microphysics scheme with explicit aerosol-cloud interactions and its performance in quantitative precipitation forecasting (QPF) in the CMA-MESO V5.0, Atmos. Res., 108649, https://doi.org/10.1016/j.atmosres.2025.108649, 2025.

Jin, H.-G., Baik, J.-J., Lee, H., and Ahmed, T.: A new warm-cloud collection and breakup parameterization scheme for weather and climate models, Atmos. Res., 272, 106145, https://doi.org/10.1016/j.atmosres.2022.106145, 2022.

Jung, J., Yu, J., Lyu, Y., Lee, M., Hwang, T., and Lee, S.: Ground-based characterization of aerosol spectral optical properties of haze and Asian dust episodes under Asian continental outflow during winter 2014, Atmos. Chem. Phys., 17, 5297–5309, https://doi.org/10.5194/acp-17-5297-2017, 2017.

Lal, D. M., Umakanth, N., Domkawale, M. A., Gopalakrishnan, V., Srivastava, M. K., and Pawar, S. D.: Association of lightning with LCL, EL, humidity at 850 mb and at 200 mb during various CAPE, over northern India, Sci. Total Environ., 915, 169947, https://doi.org/10.1016/j.scitotenv.2024.169947, 2024.

Li, C., Li, J., Dubovik, O., Zeng, Z.-C., and Yung, Y. L.: Impact of Aerosol Vertical Distribution on Aerosol Optical Depth Retrieval from Passive Satellite Sensors, Remote Sens.-Basel, 12, 1524, https://doi.org/10.3390/rs12091524, 2020.

Li, H., Liu, B. M., Ma, X., Ma, Y. Y., Jin, S. K., Fan, R. N., Wang, W. Y., Fang, J., Zhao, Y. F., and Gong, W.: The Influence of Temperature Inversion on the Vertical Distribution of Aerosols, Remote Sens.-Basel, 14, https://doi.org/10.3390/rs14184428, 2022.

Li, J., Li, C. C., Guo, J. P., Li, J., Tan, W. S., Kang, L., Chen, D. D., Song, T., and Liu, L.: Retrieval of aerosol profiles by Raman lidar with dynamic determination of the lidar equation reference height, Atmos. Environ., 199, 252–259, https://doi.org/10.1016/j.atmosenv.2018.11.048, 2019.

Li, J., Gao, W., Cao, L., Xiao, Y., Zhang, Y., Zhao, S., Liu, Z., Liu, Z., Tang, G., Ji, D., Hu, B., Song, T., He, L., Hu, M., and Wang, Y.: Significant changes in autumn and winter aerosol composition and sources in Beijing from 2012 to 2018: Effects of clean air actions, Environ. Pollut., 268, 115855, https://doi.org/10.1016/j.envpol.2020.115855, 2021a.

Li, Q., Yang, S., Cui, X.-P., and Gao, S.-T.: Investigating the initiation and propagation processes of convection in heavy precipitation over the western Sichuan Basin, Atmospheric and Oceanic Science Letters, 10, 235–242, https://doi.org/10.1080/16742834.2017.1301766, 2017.

Li, Q., Zhang, H., Cai, X., Song, Y., and Zhu, T.: The impacts of the atmospheric boundary layer on regional haze in North China, npj Climate and Atmospheric Science, 4, 9, https://doi.org/10.1038/s41612-021-00165-y, 2021b.

Li, Z., Huang, Z., Bi, J., Dong, Q., Wang, Y., Abdullaev, S. F., Nozirov, D., Li, W., Li, Z., Meng, Z., Liu, W., and Song, X.: Radiative forcing and vertical heating rate of dust aerosols in southwestern Tajikistan during summer 2023, Atmos. Environ., 345, 121051, https://doi.org/10.1016/j.atmosenv.2025.121051, 2025.

Liang, Y., Che, H., Wang, H., Zhang, W., Li, L., Zheng, Y., Gui, K., Zhang, P., and Zhang, X.: Aerosols Direct Radiative Effects Combined Ground-Based Lidar and Sun-Photometer Observations: Cases Comparison between Haze and Dust Events in Beijing, Remote Sens.-Basel, 14, 266, https://doi.org/10.3390/rs14020266, 2022.

Liu, S., Xing, J., Zhao, B., Wang, J., Wang, S., Zhang, X., and Ding, A.: Understanding of Aerosol–Climate Interactions in China: Aerosol Impacts on Solar Radiation, Temperature, Cloud, and Precipitation and Its Changes Under Future Climate and Emission Scenarios, Current Pollution Reports, 5, 36–51, https://doi.org/10.1007/s40726-019-00107-6, 2019.

Liu, S. H., Wang, H. L., Zhao, D. L., Ke, Y., Wu, Z. H., Shen, L. J., and Zhao, T. L.: Aircraft observations of aerosols and BC in autumn over Guangxi Province, China: Diurnal variation, vertical distribution and source appointment, Sci. Total Environ., 906, https://doi.org/10.1016/j.scitotenv.2023.167550, 2024.

Luo, H., Guan, Q., Shao, W., Du, Q., Xiao, X., Ni, F., and Zhang, J.: Quantifying the contribution of dust sources in the arid area of northwest China using multivariate statistical techniques and Bayesian mixing models, J. Clean. Prod., 379, 134672, https://doi.org/10.1016/j.jclepro.2022.134672, 2022.

Manavi, S. E. I., Aktypis, A., Siouti, E., Skyllakou, K., Myriokefalitakis, S., Kanakidou, M., and Pandis, S. N.: Atmospheric aerosol spatial variability: Impacts on air quality and climate change, One Earth, 8, 101237, https://doi.org/10.1016/j.oneear.2025.101237, 2025.

Marsli, I., Makaoui, A., Moussaoui, M., Mezrhab, A., and Diouri, M.: Analysis of aerosol optical properties and implications to radiative forcing over the Mediterranean Basin, E3S Web Conf., 680, 00137, https://doi.org/10.1051/e3sconf/202568000137, 2025.

Mazza, E. and Chen, S. S.: Compound Dry-Dusty Air Intrusions During the Genesis of Tropical Storm Kate (2021): Observations From the CPEX-AW Field Campaign and Coupled Modeling, J. Geophys. Res.-Atmos., 130, e2024JD042653, https://doi.org/10.1029/2024JD042653, 2025.

Meng, L., He, Q., Zhao, T., Zhang, H., Yang, X., Mamtimin, A., Yang, F., Zhou, C., and Huo, W.: Interactions between dust aerosols and the ultra-high atmospheric boundary layer: Case study of vertical observation over the Taklimakan Desert, China, Atmos. Environ., 343, 120977, https://doi.org/10.1016/j.atmosenv.2024.120977, 2025.

Nogueira, M.: Inter-comparison of ERA-5, ERA-interim and GPCP rainfall over the last 40 years: Process-based analysis of systematic and random differences, J. Hydrol., 583, 124632, https://doi.org/10.1016/j.jhydrol.2020.124632, 2020.

Noh, Y. M., Lee, H., Mueller, D., Lee, K., Shin, D., Shin, S., Choi, T. J., Choi, Y. J., and Kim, K. R.: Investigation of the diurnal pattern of the vertical distribution of pollen in the lower troposphere using LIDAR, Atmos. Chem. Phys., 13, 7619–7629, https://doi.org/10.5194/acp-13-7619-2013, 2013.

Pace, G., Junkermann, W., Vitali, L., Di Sarra, A., Meloni, D., Cacciani, M., Cremona, G., Iannarelli, A. M., and Zanini, G.: On the complexity of the boundary layer structure and aerosol vertical distribution in the coastal Mediterranean regions: a case study, Tellus B, https://doi.org/10.3402/tellusb.v67.27721, 2015.

Pal, S., Prince, N., Anand, M., and Hamel, M.: Aerosol transport and associated boundary layer thermodynamics under contrasting synoptic conditions over a semiarid site, Sci. Total Environ., 962, 178357, https://doi.org/10.1016/j.scitotenv.2024.178357, 2025.

Parajuli, S. P., Stenchikov, G. L., Ukhov, A., Shevchenko, I., Dubovik, O., and Lopatin, A.: Aerosol vertical distribution and interactions with land/sea breezes over the eastern coast of the Red Sea from lidar data and high-resolution WRF-Chem simulations, Atmos. Chem. Phys., 20, 16089–16116, https://doi.org/10.5194/acp-20-16089-2020, 2020.

Park, S. and Allen, R.: Understanding influences of convective transport and removal processes on aerosol vertical distribution, Geophys. Res. Lett., 42, https://doi.org/10.1002/2015GL066175, 2015.

Patashnick, H. and Rupprecht, E. G.: Continuous PM-10 Measurements Using the Tapered Element Oscillating Microbalance, J. Air Waste Manage., 41, 1079–1083, https://doi.org/10.1080/10473289.1991.10466903, 1991.

Petrovic, M., Radonic, J., Mihajlovic, I., Obrovski, B., Ubavin, D., Turk Sekulić, M., and Miloradov, M.: Selection of optimal parameters for future research monitoring programmes on msw landfill in novi sad, Serbia, Fresen. Environ. Bull., 26, 4867–4875, 2017.

Prasad, P., Basha, G., and Ratnam, M. V.: Is the atmospheric boundary layer altitude or the strong thermal inversions that control the vertical extent of aerosols?, Sci. Total Environ., 802, https://doi.org/10.1016/j.scitotenv.2021.149758, 2022.

Ramanathan, V., Ramana, M. V., Roberts, G., Kim, D., Corrigan, C., Chung, C., and Winker, D.: Warming trends in Asia amplified by brown cloud solar absorption, Nature, 448, 575–578, https://doi.org/10.1038/nature06019, 2007.

Reddy, K., Phanikumar, D. V., Joshi, H., Nazeer Ahammed, Y., and Naja, M.: Effect of diurnal variation of aerosols on surface reaching solar radiation, J. Atmos. Sol.-Terr. Phy., 129, 62–68, https://doi.org/10.1016/j.jastp.2015.04.011, 2015.

Ricchiazzi, P., Yang, S., Gautier, C., and Sowle, D.: SBDART: A Research and Teaching Software Tool for Plane-Parallel Radiative Transfer in the Earth's Atmosphere, B. Am. Meteorol. Soc., 79, 2101–2114, https://doi.org/10.1175/1520-0477(1998)079<2101:SARATS>2.0.CO;2, 1998.

Sarangi, C., Qian, Y., Rittger, K., Ruby Leung, L., Chand, D., Bormann, K. J., and Painter, T. H.: Dust dominates high-altitude snow darkening and melt over high-mountain Asia, Nat. Clim. Change, 10, 1045–1051, https://doi.org/10.1038/s41558-020-00909-3, 2020.

Seo, J., Kim, J. Y., Youn, D., Lee, J. Y., Kim, H., Lim, Y. B., Kim, Y., and Jin, H. C.: On the multiday haze in the Asian continental outflow: the important role of synoptic conditions combined with regional and local sources, Atmos. Chem. Phys., 17, 9311–9332, https://doi.org/10.5194/acp-17-9311-2017, 2017.

Serafin, S., Adler, B., Cuxart, J., De Wekker, S., Gohm, A., Grisogono, B., Kalthoff, N., Kirshbaum, D., Rotach, M., Schmidli, J., Stiperski, I., Večenaj, Ž., and Zardi, D.: Exchange Processes in the Atmospheric Boundary Layer Over Mountainous Terrain, Atmosphere-Basel, 9, 102, https://doi.org/10.3390/atmos9030102, 2018.

Shivkumar, M., Dhanya, G., Ganesh, K. E., Pranesha, T. S., Sudhindra, K. R., Chate, D., and Beig, G.: Temporal variability of $PM_{2.5}$ and its possible sources at the tropical megacity, Bengaluru, India, Environ. Monit. Assess., 194, https://doi.org/10.1007/s10661-022-10235-0, 2022.

Smirnov, A., Holben, B. N., Eck, T. F., Slutsker, I., Chatenet, B., and Pinker, R. T.: Diurnal variability of aerosol optical depth observed at AERONET (Aerosol Robotic Network) sites, Geophys. Res. Lett., 29, https://doi.org/10.1029/2002gl016305, 2002.

Song, J., Xia, X., Che, H., Wang, J., Zhang, X., and Li, X.: Daytime variation of aerosol optical depth in North China and its impact on aerosol direct radiative effects, Atmos. Environ., 182, 31–40, https://doi.org/10.1016/j.atmosenv.2018.03.024, 2018.

Song, X., Zhou, T., Wang, Y., Li, X., Wu, D., Gu, Y., Lin, Z., Abdullaev, S., and Amonov, M.: Spatiotemporal evolution of dust over Tarim Basin under continuous clear-sky, Atmos. Res., 312, 107764, https://doi.org/10.1016/j.atmosres.2024.107764, 2024.

Stein, A., Draxler, R., Rolph, G., Stunder, B., Cohen, M., and Ngan, F.: NOAA's HYSPLIT Atmospheric Transport and Dispersion Modeling System, B. Am. Meteorol. Soc., 96, 2059–2077, https://doi.org/10.1175/BAMS-D-14-00110.1, 2016.

Su, B., Li, H., Zhang, M., Bilal, M., Wang, M., Atique, L., Zhang, Z., Zhang, C., Han, G., Qiu, Z., and Ali, M. A.: Optical and Physical Characteristics of Aerosol Vertical Layers over Northeastern China, Atmosphere-Basel, 11, 501, https://doi.org/10.3390/atmos11050501, 2020a.

Su, T., Li, Z., Li, C., Li, J., Han, W., Shen, C., Tan, W., Wei, J., and Guo, J.: The significant impact of aerosol vertical structure on lower atmosphere stability and its critical role in aerosol–planetary boundary layer (PBL) interactions, Atmos. Chem. Phys., 20, 3713–3724, https://doi.org/10.5194/acp-20-3713-2020, 2020b.

Sun, T., Che, H., Qi, B., Wang, Y., Dong, Y., Xia, X., Wang, H., Gui, K., Zheng, Y., Zhao, H., Ma, Q., Du, R., and Zhang, X.: Aerosol optical characteristics and their vertical distributions under enhanced haze pollution events: effect of the regional transport of different aerosol types over eastern China, Atmos. Chem. Phys., 18, 2949–2971, https://doi.org/10.5194/acp-18-2949-2018, 2018.

Tutsak, E. and Koçak, M.: Optical and microphysical properties of the columnar Aerosol burden over the Eastern Mediterranean: Discrimination of Aerosol types, Atmos. Environ., 229, 117463, https://doi.org/10.1016/j.atmosenv.2020.117463, 2020.

Valenzuela, A., Costa, M. J., Rascado, J. L., Bortoli, D., and Olmo, F.: Solar and thermal radiative effects during the 2011 extreme desert dust episode over Portugal, Atmos. Environ., 148, https://doi.org/10.1016/j.atmosenv.2016.10.037, 2016.

Wang, X., Liu, M., Luo, L., Chen, X., Zhang, Y., Zhang, H., Yang, S., and Li, Y.: Spatial and Temporal Distributions of Air Pollutants in Nanchang, Southeast China during 2017–2020, Atmosphere-Basel, 12, 1298, https://doi.org/10.3390/atmos12101298, 2021.

Wang, Y., Yu, M., Wang, Y., Tang, G., Song, T., Zhou, P., Liu, Z., Hu, B., Ji, D., Wang, L., Zhu, X., Yan, C., Ehn, M., Gao, W., Pan, Y., Xin, J., Sun, Y., Kerminen, V.-M., Kulmala, M., and Petäjä, T.: Rapid formation of intense haze episodes via aerosol–boundary layer feedback in Beijing, Atmos. Chem. Phys., 20, 45–53, https://doi.org/10.5194/acp-20-45-2020, 2020.

Wang, Y., Zhou, T., Song, X., Li, X., Wu, D., Gu, Y., Wang, J., Wei, L., Lin, Z., Chen, R., and Gong, C.: The Role of Nocturnal Low-Level Jets on Persistent Floating Dust over the Tarim Basin, Atmosphere-Basel, 17, 134, https://doi.org/10.3390/atmos17020134, 2026.

Wang, Y. H., Liu, Z. R., Zhang, J. K., Hu, B., Ji, D. S., Yu, Y. C., and Wang, Y. S.: Aerosol physicochemical properties and implications for visibility during an intense haze episode during winter in Beijing, Atmos. Chem. Phys., 15, 3205–3215, https://doi.org/10.5194/acp-15-3205-2015, 2015.

Wen, Q., Li, Y., Du, M., Song, W., Wei, L., Wang, Z., and Li, X.: Interdecadal shift in the impact of winter land–sea thermal contrasts on following spring transcontinental dust transport pathways in North Africa, Atmos. Chem. Phys., 25, 10853–10867, https://doi.org/10.5194/acp-25-10853-2025, 2025.

Xiang, Y., Zhang, T., Liu, J., Wan, X., Loewen, M., Chen, X., Kang, S., Fu, Y., Lv, L., Liu, W., and Cong, Z.: Vertical profile of aerosols in the Himalayas revealed by lidar: New insights into their seasonal/diurnal patterns, sources, and transport, Environ. Pollut., 285, https://doi.org/10.1016/j.envpol.2021.117686, 2021.

Xie, H., Zhou, T., Fu, Q., Huang, J., Huang, Z., Jianrong, B., Shi, J., Zhang, B., and Ge, J.: Automated detection of cloud and aerosol features with SACOL micro-pulse lidar in northwest China, Opt. Express, 25, 30732, https://doi.org/10.1364/OE.25.030732, 2017.

Yang, L., Zhou, T., Yang, X., Huang, Z., Wang, L., Li, X., Yang, Y., and Tao, H.: Study on a sand and dust process based on lidar network, Journal of Atmospheric and Environmental Optics, 20, 752–765, https://doi.org/10.3969/j.issn.1673-6141.2025.06.006, 2025.

Yang, X., Peng, J., Liu, B., and Liu, Y.: Multi-Scale Analysis of Grain Size in the Component Structures of Sediments Accumulated along the Desert-Loess Transition Zone of the Tengger Desert and Implications for Sources and Aeolian Dust Transportation, Atmosphere-Basel, 15, 239, https://doi.org/10.3390/atmos15020239, 2024.

Yim, S. H. L. and Huang, T.: Analysis of the air quality in upper atmospheric boundary layer in a high-density city in Asia using 3 year vertical profiles measured by the 3-Dimensional Real-Time Atmospheric Monitoring System (3DREAMS), Sci. Total Environ., 857, https://doi.org/10.1016/j.scitotenv.2022.159137, 2023.

Yorks, J. E., Wang, J., McGill, M. J., Follette-Cook, M., Nowottnick, E. P., Reid, J. S., Colarco, P. R., Zhang, J., Kalashnikova, O., Yu, H., Marenco, F., Santanello, J. A., Weckwerth, T. M., Li, Z., Campbell, J. R., Yang, P., Diao, M., Noel, V., Meyer, K. G., Carr, J. L., Garay, M., Christian, K., Bennedetti, A., Ring, A. M., Crawford, A., Pavolonis, M. J., Aquila, V., Kim, J., and Kondragunta, S.: A SmallSat Concept to Resolve Diurnal and Vertical Variations of Aerosols, Clouds, and Boundary Layer Height, B. Am. Meteorol. Soc., 104, E815–E836, https://doi.org/10.1175/BAMS-D-21-0179.1, 2023.

Zhang, Q., Zhao, Y.-d., Wang, S., and Ma, F.: A Study on Atmospheric Thermal Boundary Layer Structure in Extremely Arid Desert and Gobi Region on the Clear Day in Summer, Advances in Earth Science, 22, 1150, http://www.adearth.ac.cn/CN/10.11867/j.issn.1001-8166.2007.11.1150, 2007.

Zhang, Q., Hu, W., Ren, H., Yang, J., Deng, J., Wang, D., Sun, Y., Wang, Z., Kawamura, K., and Fu, P.: Diurnal variations in primary and secondary organic aerosols in an eastern China coastal city: The impact of land-sea breezes, Environ. Pollut., 319, https://doi.org/10.1016/j.envpol.2023.121016, 2023a.

Zhang, X. L., Zheng, Y., Che, H. Z., Gui, K., Li, L., Zhao, H. J., Liang, Y. X., Yao, W. R., Zhang, X. D., Zhao, H. H., Lu, Y. T., and Zhang, X. Y.: Seasonal and Diurnal Characteristics of the Vertical Profile of Aerosol Optical Properties in Urban Beijing, 2017–2021, Remote Sens.-Basel, 15, https://doi.org/10.3390/rs15020475, 2023b.

Zhao, C., Sun, Y., Yang, J., Li, J., Zhou, Y., Yang, Y., Fan, H., and Zhao, X.: Observational evidence and mechanisms of aerosol effects on precipitation, Sci. Bull., 69, 1569–1580, https://doi.org/10.1016/j.scib.2024.03.014, 2024.

Zhong, J., Zhang, X., Dong, Y., Wang, Y., Liu, C., Wang, J., Zhang, Y., and Che, H.: Feedback effects of boundary-layer meteorological factors on cumulative explosive growth of $PM_{2.5}$ during winter heavy pollution episodes in Beijing from 2013 to 2016, Atmos. Chem. Phys., 18, 247–258, https://doi.org/10.5194/acp-18-247-2018, 2018.

Zhou, T., Xie, H., Jianrong, B., Huang, Z., Huang, J., Shi, J., Zhang, B., and Zhang, W.: Lidar Measurements of Dust Aerosols during Three Field Campaigns in 2010, 2011 and 2012 over Northwestern China, Atmosphere-Basel, 9, https://doi.org/10.3390/atmos9050173, 2018.

Zhou, T., Xie, H., Jiang, T., Huang, J., Bi, J., Huang, Z., and Shi, J.: Seasonal characteristics of aerosol vertical structure and autumn enhancement of non-spherical particle over the semi-arid region of northwest China, Atmos. Environ., 244, 117912, https://doi.org/10.1016/j.atmosenv.2020.117912, 2021.

Zhou, T., Zhou, X., Yang, Z., Córdoba-Jabonero, C., Wang, Y., Huang, Z., Pengbo, D., Luo, Q., Zhang, Z., Shi, J., Jianrong, B., and Ali-Khodja, H.: Transboundary transport of non-east and East Asian dust observed at Dunhuang, northwest China, Atmos. Environ., https://doi.org/10.1016/j.atmosenv.2023.120197, 2024.